Mineralogical transformations in polymetallic nodules and the change of Ni, Cu and Co crystal-chemistry upon burial in sediments

Anna Wegorzewski, Sylvain Grangeon, Samuel Webb, Christina Heller, Thomas Kuhn

Mineralogical transformations in polymetallic nodules and the change of Ni, Cu and Co crystal-chemistry upon burial in sediments

Anna V. Wegorzewski[a], Sylvain Grangeon[b], Samuel M. Webb[c], Christina Heller[a], and Thomas Kuhn[a]

[a] Federal Institute for Geoscience and Natural Resources (BGR), Stilleweg 2, D-30655 Hannover, Germany. Anna.Wegorzewski@bgr.de

[b] BRGM, 3 Avenue Claude Guillemin, 45060 Orléans cedex 2, France

[c] Stanford Synchrotron Radiation Laboratory, Menlo Park, California 94025, U.S.A.

Abstract

Polymetallic nodules from the Clarion-Clipperton Zone of the equatorial Pacific Ocean were studied using X-ray diffraction, X-ray absorption, Fourier-transformed infrared spectroscopy and transmission electron microscopy. This study includes nodules found at the sediment surface as well as subsurface (14-16 cm sediment depth) and deeply buried (530-985 cm sediment depth) nodules. The surface and subsurface nodules are currently under oxic conditions whereas the deeply buried nodules are under suboxic conditions. Surface nodules consist mainly of turbostratic phyllomanganates (7 Å and 10 Å vernadite and Fe-vernadite); todorokite is a minor phase, if present at all. In contrast, subsurface and especially deeply buried nodules predominantly consist of todorokite, which increases in abundance with depth in the sediment. Thus, upon burial of nodules within the shallow sediment, phyllomanganates transform to todorokite, probably through the combined action of time and change in the ambient chemical conditions. Nodules from deeper sediment depth (>500 cm) consist primarily of todorokite and additionally show signs of dissolution.

The transformation of phyllomanganates to todorokite and their further dissolution upon nodule burial under suboxic conditions induces modifications in the crystal-chemistry of Ni, Co, and Cu. In surface nodules, Ni and Co are incorporated in the octahedral sheets of phyllomanganates, whereas Cu is located at the crystal edges of those phyllomanganate sheets. In buried nodules Cu and to a lesser extent Ni are incorporated in todorokite by forming outer-sphere complexes within the tunnels. However, Ni is predominantly

incorporated within the octahedra of the newly formed todorokite structure. Co is also enriched in the octahedra of todorokite as a result of dissolution of hydrogenetic vernadite and re-incorporation in the more stable Mn-phases formed during the diagenetic transformation. Co enrichment under suboxic conditions after burial within the sediments is noteworthy since Co in surface nodules is characteristic for oxic conditions.

Keywords: manganese nodules, phyllomanganate, todorokite, hydrogenetic, suboxic-diagenetic, cobalt, nickel, copper, XRD, IR, EXAFS

1. INTRODUCTION

Manganese (Mn) nodules are Mn-Fe oxy-hydroxide concretions occurring in almost all oceans, at water depths between approximately 3000 and 6000 m (e.g., Halbach et al., 1988; Koschinsky and Halbach 1995, Hein et al., 2013; Kuhn et al., 2017a). Mn-nodules are potential resources for Fe, Mn, Ni, Cu, Co, Zn, Mo as well as rare earth elements (REE; e.g., Halbach et al., 1988; Hein et al., 2013; Hein and Koschinsky, 2013).

In general, Mn-nodules form on the sediment surface or within the first few centimeters of the sediment (Halbach et al., 1988). They are made up of individual nm- to µm-thick layered growth structures (LGS), which grow around a nucleus (e.g., rock fragments, shark teeth; Halbach et al., 1988). Individual LGS are the result of hydrogenetic (oxic) and/or suboxic-diagenetic precipitation.

Hydrogenetic LGS form by Mn and Fe precipitation from oxygen-rich seawater (oxic; Halbach et al., 1988; Koschinsky and Halbach 1995) as well as from oxic sediment pore water (Wegorzewski and Kuhn 2014; Kuhn et al., 2017a). Oxic diagenesis is characterized by redox potentials of around +490 mV, the presence of oxygen, low amounts of dissolved manganese (few $\mu g \cdot l^{-1}$) and nitrate formation within the environment (nitrification; Halbach et al., 1988).

Hydrogenetic LGS generate dense layers with columnar growth structures and are characterized by Mn/Fe ratios of <4 as well as low Ni (0.46±0.24 wt.%) and Cu (0.34±0.16 wt.%) contents, but high Co (0.30±0.12 wt.%) and REE (~800 ppm) contents (Halbach et al., 1988; Wegorzewski and Kuhn 2014; Kuhn et al., 2017a). The preferential association of a given element with Mn or Fe oxide phases might result from its aqueous speciation, as Mn oxides are generally negatively charged under sea water conditions, whereas Fe oxy-hydroxides are neutral or slightly positively charged (Koschinsky and Halbach 1995). Mineralogically, hydrogenetic LGS consist of turbostratic Fe-vernadite (δ-MnO_2) that is

epitaxially intergrown with an amorphous δ-FeOOH phase (Koschinsky and Halbach 1995; Hein et al., 2013; Wegorzewski et al., 2015).

Suboxic-diagenetic LGS are formed by metal precipitation from suboxic near-bottom sea water and/or sediment pore water (Halbach et al., 1988; Koschinsky and Halbach 1995; Wegorzewski and Kuhn 2014). The suboxic conditions for LGS formations are characterized by low or even zero oxygen concentrations (<5 μmol $O_2 \cdot l^{-1}$; Hein and Koschinsky 2014), a redox potential of around +330 mV, nitrate reduction (denitrification), and the occurrence of dissolved manganese (Halbach et al., 1988). Under these suboxic conditions, Mn^{4+} can be reduced but no Fe^{3+} reduction and dissolution occurs. Suboxic-diagenetic LGS have Mn/Fe ratios of 5 – 800, Ni and Cu amounts reaching up to ~4 wt.%, but low Co (0.08±0.08 wt.%) and REE (<600 ppm) concentrations (Koschinsky and Halbach 1995; Wegorzewski and Kuhn 2014; Kuhn et al., 2017a). Mineralogically, they consist of 7 Å and 10 Å vernadite, where the numbers refer to the phyllomanganate layer-to-layer distance. Occurrences of todorokite in marine Mn-nodules from the sediment surface of the Clarion and Clipperton Zone (CCZ) are scarce (e.g., Manceau et al., 2014; Wegorzewski et al., 2015; Bodeï et al., 2007; Manceau et al., 2014; Atkins et al., 2016).

Studying the mineralogy of marine Mn-nodules (Burns and Burns, 1978a; Manceau et al., 2014; Peacock and Sherman, 2007a,b; Peacock 2009) is difficult, because the minerals are poorly crystalline, intermixed with each other on a nm scale (Burns and Burns 1977; Usui and Terashima, 1997; Atkins et al., 2016), and have overlapping diffraction peaks (Post and Bish, 1988; Bodeï et al., 2007; Manceau et al., 2014). Additional complexity results from the topotactic relation between phyllomanganates and todorokite (Bodeï et al., 2007; Pal´chick et al., 2011; Manceau et al., 2014).

The chemical and mineralogical composition of individual LGS reflects the environmental conditions within which the nodules grew (e.g., Wegorzewski and Kuhn, 2014; Koschinsky and Hein, 2017). However, secondary transformation of primary LGS over time may also occur (Wegorzewski and Kuhn, 2014; Blöthe et al., 2015). Indeed, because of the high porosity (up to 60%) and permeability of the nodules (Blöthe et al., 2015), surrounding water can penetrate the nodules and induce mineralogical changes if the water chemistry changes with time (for example as a result of climate cycles).

Nodules do not only occur on the sediment surface, but they are also found buried within the sediment column. Buried nodules have been sampled sporadically in the Pacific, Atlantic and Indian Oceans (Cronan and Tooms, 1967; Banerjee et al., 1991; Heye et al., 1979; Pattan and Parthiban, 2007). Heller et al., (2018) documented the occurrence of buried nodules down to

~10 m sediment depth within siliceous ooze of the eastern CCZ in the central Pacific Ocean. The authors distinguished between nodules buried at shallow depth (subsurface nodules; < 100 cm) currently under oxic conditions and nodules buried at greater depths (deeply buried nodules; > 500 cm) currently under suboxic conditions (Heller et al., 2018).

Nodules buried within the sediment column differ from surface ones in the occurrence of individual LGS as well as in their chemical composition (Heller et al., 2018). Compared to surface nodules, buried nodules are depleted in Ni, Zn, Mo, and Li whereas they are enriched in Co, W, and Te. Mn, Cu, V, and Ba have about the same concentration in both types of nodules (Heller et al., 2018). Furthermore, there is an additional type of layer growth structure in buried nodules that has not been found in surface nodules. This growth structure has high contents of Fe and is rich in Si and Al, but has low trace metal concentrations (Heller et al., 2018). The fate of nodules during their burial process is unclear. Do nodules continue to grow further, stop growing, or do they dissolve? Heller et al., (2018) showed that Mn-nodules buried in suboxic deep-sea sediments are subject to diagenetic processes induced by reactions with the surrounding pore water. These diagenetic processes affect the geochemical composition of the nodules as well as the surrounding sediments (Heller et al., 2018). The results of this study are the continuation of the previous work by Heller et al., (2018), but focus on the mineralogy and the crystal-chemistry of Ni, Cu, and Co in nodules from the sediment surface in comparison with buried ones. The overall aim of this study is to determine how Mn minerals and associated metals evolve with time and burial.

2. MATERIAL AND EXPERIMENTAL METHODS

2.1 Material

Samples were recovered during RV *SONNE* cruises SO205 (in 2010) and SO240 (in 2015) within the eastern Clarion and Clipperton Zone in the Pacific Ocean (Rühlemann et al., 2011; Kuhn et al., 2015). Figure 1 shows a bathymetric map of the study area with sample locations (Kuhn et al., 2015). Samples were collected from the sediment surface (using a box corer (KG); SO205-32KG, SO205-44KG, SO205-68KG, SO240-21KG) in water depths between 4200 and 4500 m (Rühlemann et al., 2011; Kuhn et al., 2015), as well as from different sediment depths using a box corer (SO240-107KG-16cm), piston corer (KL: SO240-09KL-14-16cm, SO240-22KL-530cm, SO240-22KL-801cm, SO240-09KL-837cm), and gravity corer (SL: SO240-65SL-985cm). Buried nodules were collected in sediment cores that were taken where hydroacoustic data showed a change in the density of the sediment between 500

and 1000 cm depth (BGR data; Rühlemann et al., 2018). Detailed descriptions of the study area can be found in Rühlemann et al. (2011; 2018) and Kuhn et al. (2015). Different nodule types (surface nodules, subsurface nodules (<100 cm) and deeply buried nodules (>500 cm; Heller et al., 2018)) were chosen for further detailed mineralogical and crystal-chemical investigations. For a more detailed description of the chemistry of the buried nodules see Heller et al. (2018).

2.2 Electron probe microanalyzer (EPMA)

Chemical mappings were performed with an electron probe microanalyzer (EPMA: JEOL JXA-8530F). Samples were prepared as polished thin sections (~50 µm thick). Manganese, Fe, Ni, and Cu were mapped using energy dispersive X-ray spectrometry and Co using wavelength-dispersive X-ray spectrometry (WDX). The beam size was 3-5 µm and the dwell time was 500 ms. The accelerating voltage was set to 15 kV and a beam current of 20 nA was used. In addition to the mapping, individual point analyses were conducted to better quantify metal contents of individual growth structures. For a detailed description of the EPMA measurements see Wegorzewski and Kuhn (2014).

2.3 X-ray diffraction (XRD)

Mineralogy was determined for three bulk nodules from the sediment surface (44KG, 68KG, 21KG-1), three nodules from the subsurface (107KG-16cm, 107KG-36cm; 09KL-14-16cm) and four nodules from greater sediment depths (22KL-530cm, 22KL-801cm, 09KL-837cm, 65SL-985cm).

Nodules were cut in half and one complete half was ground in a planetary sphere mill (Retsch PM 11 CM; ≤50 µm particle size). Powder XRD patterns were collected using a PANalytical X´Pert PRO MPD θ-θ diffractometer (Cu-Kα radiation generated at 40 kV and 30 mA), equipped with a variable divergence slit (20 mm irradiated length), primary and secondary soller slits, Scientific X´Celerator detector (active length 2.122°; phd 60), and a sample changer (sample diameter 26 mm). Samples were scanned over 5° to 85° 2θ with a step size of 0.0334° 2θ and a measuring time of 200 sec per step.

To distinguish between todorokite and 10 Å phyllomanganates, nodule powder was analyzed twice, after drying at 40°C and after drying at 105°C (Uspenskaya et al., 1987; Manceau et al., 2014). Upon drying at 105°C, 10 Å phyllomanganates such as buserite loose interlayer

164 water and collapse, thus reducing the layer-to-layer distance and the corresponding diffraction
165 peak to ~7 Å. In contrast, the 10 Å reflection of todorokite remains unchanged upon heating
166 at 105 °C.
167

168 **2.4 Transmission electron microscopy (TEM)**

169 Slices from layers of buried nodule 22KL-801cm were cut using a focused ion beam
170 preparation technique (FIB) at the GeoForschungsZentrum, Potsdam (Wirth; 2009). Different
171 growth structures of interest were selected for sampling based on EPMA analyses. The
172 sampled foils (15 x 10 x 0.150 µm) were sputtered from the target material using Ga-ions
173 with energy of 30 keV (Wirth; 2009). For high-resolution transmission electron microscopy
174 foils were taken from the excavation sites applying the so-called lift-out technique (Giannuzzi
175 et al. 1997). Detailed description of the FIB technique is given in Giannuzzi et al. (2005) and
176 Wirth (2004; 2009). TEM analyses were carried out using a Philips CM20 operated at 200
177 kV.
178

179 **2.5 Extended X-ray absorption fine structure (EXAFS) spectroscopy**

180 EXAFS experiments were conducted at the Stanford Synchrotron Radiation Lightsource
181 (SSRL). Ni and Cu *K*-edge X-ray absorption spectroscopy was carried out on bulk nodules
182 [surface nodules, subsurface nodules (14 – 16cm) and deeply buried nodules (530 – 985cm)].
183 Ni and Cu *K*-edge EXAFS analyses of bulk nodules (powder samples) were performed at
184 beam line 4-1 using a Si (220) double crystal monochromator calibrated to 8979 eV with a
185 Cu(0) foil and to 8333 eV with a Ni(0) foil. Sample powders were fixed to polyimide tape on
186 the sample holder. X-ray absorption spectra were averaged before analysis for better statistics.
187 Co *K*-edge EXAFS analyses were performed on thin sections at beam line 10-2. High-
188 resolution XRF maps were collected prior to EXAFS measurements to identify regions of
189 interest. Additional Co *K*-edge X-ray absorption spectroscopy was carried out on different
190 individual Co rich areas of suboxic-diagenetic LGS in one deep buried nodule (22KL-801cm).
191 X-ray absorption data for Co were recorded over the energy range of 7479 to 8315 eV. The
192 incorporation mechanism of Co in vernadite (δ-MnO_2) within hydrogenetic LGS of surface
193 nodules has been thoroughly studied (e.g., Manceau et al., 2014) and was not determined in
194 this study. Individual Co EXAFS spectra were averaged together to improve counting
195 statistics as they were noted to have similar features.

196 The storage ring energy during the measurements was 3.0 GeV and the beam current was
197 maintained at ~500 mA in top-off mode. The X-ray absorption spectra were normalized using
198 the software Athena and the EXAFS spectra were Fourier-filtered afterwards (Ravel and
199 Newville, 2005). The EXAFS spectra were k^3-weighted and converted to R-space by fast
200 Fourier transformation over the k range of 2.5-12 A^{-1} using a Kaiser-Bessel window with the
201 windowing parameter (dk) set to 3 A^{-1} (Peña et al., 2015).
202

203 **2.6 Fourier-transformed infrared spectroscopy (FTIR)**

204 Mid- (MIR) and far- (FIR) infrared spectra were collected on pellets made of 1 mg of sample
205 mixed with 200 mg of KBr. The analyses were conducted on a Thermo Nicolet Nexus FTIR
206 spectrometer (MIR beam splitter KBr, detector DTGS TEC; FIR beam splitter solid substrate,
207 detector DTGS PE) at the BGR laboratory. The resolution was adjusted to 2 cm^{-1}.
208

209 **3. RESULTS**

210 **3.1 Element associations in surface and buried nodules**

211 EPMA maps show different Ni, Cu, and Co associations in surface (e.g., 32KG) and deeply
212 buried nodules (e.g., 22KL-801cm; Figs. 2a-f and 3a-f). In nodules from the sediment surface,
213 two types of LGS can be recognized: one is enriched in Mn (20 - 51 wt.%) and depleted in Fe
214 (0.5 - 3 wt.%), and the other is enriched in Fe (4 – 23wt.%) and has Mn concentrations
215 ranging from 7 to 37 wt.% (Fig. 2b,c). Ni and Cu are enriched in Mn-rich LGS, which is
216 typical for suboxic-diagenetic growth (Fig. 2a,d,e; Halbach et al., 1988; Wegorzewski and
217 Kuhn, 2014). LGSs showing columnar growth and low reflectivity (Fig. 2a) are enriched in Fe
218 (~17 wt.%) as well as Mn (~23 wt.%; Fig. 2d,e). This type of LGS is typical of hydrogenetic
219 growth, and those layers are enriched in Co (0.3 wt.%; Fig. 2f), but depleted in Ni (~0.4
220 wt.%) and Cu (~0.3 wt.%). This metal association is systematically observed in all surface
221 nodules from the eastern German license area within the CCZ (Wegorzewski and Kuhn,
222 2014).
223 In addition to the hydrogenetic and suboxic-diagenetic LGS, deeply buried nodules (e.g.,
224 22KL-801cm) contain another LGS of low reflectivity (Fig. 3a) that is enriched in Fe (14
225 wt.%), Si (20 wt.%) and Al (2.2 wt.%) but depleted in Mn (0.5 wt.%; Fig. 3b,c; also Heller et
226 al., 2018). Detailed investigations here show that this LGS is not homogenous but rather a

mixture of different materials, Fe-Si rich material is mixed with hydrogenetic material (Fig. 4).

In deeply buried nodules, Cu (0.6 – 1.8 wt.%) as well as Ni (0.3 – 2.3 wt.%) are still strongly associated with Mn within the suboxic-diagenetic LGS (Fig. 3b,d,e). In contrast to surface nodules, Co is also enriched in suboxic-diagenetic LGS (Co 0.2 – 1.2 wt.%; Fig. 3f), and the hydrogenetic layers (0.3 wt.%; Halbach et al., 1988; Wegorzewski and Kuhn 2014). Co, Cu, and Ni are unevenly distributed within the suboxic-dendritic LGS as in surface nodules but are predominantly enriched at the rim of the LGS in contact with the pores and the Fe-rich LGS (Fig. 3d-f).

3.2 Mineralogy

3.2.1 XRD and TEM

The XRD patterns of surface, subsurface and deeply buried nodules are shown in Fig. 5. The patterns of surface nodules have diffraction peaks at ~10 Å (assigned to be the 001 reflection) and ~5 Å (002 reflection of the same mineral) as well as weak peaks at ~ 7 Å (001 reflection of another mineral) and ~3.5 Å (002 reflection of this second mineral). Furthermore, two *hk* bands at ~2.45 Å (10 band) and ~1.42 Å (11 band) can be distinguished. This pattern is typical for turbostratic phyllomanganates. The layer symmetry of this mineral is hexagonal as the calculated ratio of the *d*-spacings of the two *hk* bands is ~1.73 (close to $\sqrt{3}$) and the band at 1.42 Å is almost symmetrical (e.g., Drits et al., 1997; Bodeï et al., 2007; Drits et al., 2007). Since the 002 reflection is of lower intensity than the 001 reflection, the presence of significant amounts of asbolane is unlikely.

Buried nodules (subsurface and deeply buried nodules) show diffraction peaks at ~10 Å and ~5 Å, which are sharper and of higher intensity (especially for the deeply buried nodules) than those of the surface nodules. The 7 Å reflection is much weaker compared to nodules from the surface and in some samples this reflection is almost absent (e.g., 09KL-837cm in Fig. 5). Furthermore, in buried nodules, a splitting of the *hk* band around 2.45 Å (~2.45 Å and ~2.40 Å) is observed, and additional reflections are observed between 2.2 and 1.5 Å. The ~2.45 Å and ~2.40 Å peaks are more intense in deeply buried nodules than in subsurface nodules. Other sharp peaks match the patterns of different minerals such as quartz, feldspars and phillipsite (Fig. 5).

After drying the samples at 105 °C, the ~10 Å reflection of surface nodules decrease, concomitant with an increase of the 7 Å peak. Only a small broad hump remains around ~9 Å, if at all. The *hk* bands are unaffected by drying (e.g., 21KG; Fig. 5). These results confirm that

the ~10 Å phase of surface nodules is mainly, if not purely, a turbostratic phyllomanganate and not a tectomanganate such as todorokite. In contrast, subsurface and deeply buried nodules are less affected by dehydration. The reflection shifts from ~9.7 Å to ~9.4 Å after drying at 105°C and slightly decreases in intensity but there is not a simultaneous increase of the ~7 Å reflection. This, together with the presence of two peaks at 2.45 Å and ~2.40 Å, is indicative of the presence of todorokite (e.g., Manceau et al., 2014). The fact that the ~2.40 Å peak is better defined in deeply buried nodules than in shallow buried nodules suggests an increase in todorokite crystallinity or abundance with prevailing time under suboxic conditions, sediment depth and (or) nodule ageing. Consistently, TEM micrographs (Fig. 6a,b) show the presence of tectomanganates intermixed with phyllomanganates in dendritic growth structures close to Fe-rich LGS (Fig. 6a,b) of a deeply buried nodule (22KL-801cm). The tunnel sizes of the tectomanganates vary and are locally higher than the typical 3x3 octahedra of todorokite. Due to the varied tunnel sizes (3 x >3) in this Mn mineral, it will be referred to here as "defective todorokite" (Bodeï et al., 2011).

3.2.3 FTIR

FTIR spectra of surface and buried nodules are presented in Fig. 7. FTIR bands in the region between 800 and 400 cm^{-1} are characteristic for Mn-O lattice vibrations (Kang et al., 2007). Surface nodules have three FTIR bands around 430 (weak), ~466 (strong), and 512-526 (medium strong) cm^{-1}. Subsurface nodules also display a very weak shoulder around 430 cm^{-1}, and two medium strong peaks, in the range of 457 and 468 cm^{-1} and the other between 512 and 526 cm^{-1}. These three bands are in good agreement with the IR characteristics of layered manganese oxides (Potter and Rossman, 1979; Golden et al., 1986; Kang et al., 2007). Infrared bands of buried nodules are somewhat different between 500 and 400 cm^{-1} compared to surface nodules and they have an additional band at ~760 cm^{-1} which is absent in nodules from the sediment surface (Fig. 7). According to Julien et al. (2004) and Atkins et al. (2014) the band at ~760 cm^{-1} is due to an asymmetrical Mn-O stretching vibration corresponding to corner-sharing MnO_6 octahedra and is therefore characteristic for a tectomanganate structure such as todorokite. Collectively, our data indicate that buried nodules contain tectomanganates while surface nodules mainly contain phyllomanganates.

3.3 EXAFS Results and Interpretation

3.3.1 Ni *K*-edge EXAFS

Ni *K*-edge EXAFS and the corresponding Fourier transforms (FT) are shown in Figure 8a and 8b and the modeling results are summarized in Table 1. All *k*-space data of surface and subsurface nodules are similar. In contrast, those from deeply buried nodules, and especially sample 22KL-801cm and 65SL-985cm, differ in the 6 - 7 $Å^{-1}$ region (Fig. 8a). According to Manceau et al., 2007 the decrease in the oscillation of the Ni *K*-edge EXAFS in the region between 6 and 7 $Å^{-1}$ is characteristic for higher amounts of Mn^{3+} in the octahedral sheets. This matches our mineralogical data, which show that deeply buried nodules have todorokite as the main mineral phase, which generally has a higher amount of Mn^{3+} in the structure than phyllomanganates (e.g., Bodeï et al., 2007).

The FT of all samples (surface, subsurface and buried nodules; Fig. 8b) have a peak at $R+\Delta R$ ≈1.6 Å corresponding to the first shell of O atoms around the absorbing atom (Ni-O; Peacock and Sherman 2007a, b) that can be modeled with a shell of 6 O atoms at 2.01 – 2.05 Å (Table 1). The second peak (Ni-Mn) in the FT spectra of surface and subsurface nodules is located at $R+\Delta R$ ≈ 2.41 – 2.45 Å (Fig. 8b). This peak was modeled with a shell of up to 6 Mn atoms at 2.84 – 2.87 Å (Table 1), typical for Ni structurally incorporated in the octahedral layers of phyllomanganates (^{E}Ni; Peacock and Sherman, 2007b; Manceau et al., 2014). A small peak is also observed in the FT of Ni of surface nodules at R+ΔR ~3.1-3.2 Å and could possibly be attributed to Ni sorbed as a triple-corner (^{Tc}Ni) sharing complex over vacancies of phyllomanganates or to Ni at the edges of the triple chains of a minor todorokite phase (e.g., Manceau et al., 2014; Bodeï et al., 2007). However, attempts to quantify this component by data modeling led to a proportion of 15 % of the total Ni in sample 44KG (Table 1), which is within the typical uncertainty (~20 %) of EXAFS data analysis. Thus, in the following discussion, we will make the assumption that Ni of surface and subsurface nodules from our working area is mainly incorporated within the octahedral sheets of the phyllomanganates.

These results are in good agreement with previous Ni-EXAFS studies on phyllomanganates in marine nodules and synthetic Ni-rich phyllomanganates such as birnessite (Peacock and Sherman, 2007a, b; Manceau et al., 2007; Manceau et al., 2014; Atkins et al., 2016).

In buried nodules, the FT peak at $R+\Delta R$ ≈ 2.39 – 2.45 Å is less pronounced than in surface nodules. Moreover, the peak intensity decreases with burial depth (subsurface to deeply buried nodules; Fig. 8b). This suggests a decrease in the relative abundance of Ni incorporated within the phyllomanganate sheets and/or lower amounts of neighbors around the Ni atoms within the MnO_2 sheets. Data modeling of deeply buried nodules indicate that 35 – 76 % of Ni is incorporated in the phyllomanganate sheets (^{E}Ni). The remaining fraction is bound as a triple corner (^{TC}Ni) complex over vacancies of phyllomanganates or is

incorporated within the edge of triple chains of todorokite, which is the main Mn-phase in deeply buried nodules. In both cases the binding distances are expected to be 3.5 Å – 3.6 Å (Peacock and Sherman 2007; Manceau et al., 2014). In our models, the modeled distance was 3.55 - 4.00 Å, but the number of neighbors was low (1 - 4; Table 1). In addition the FT data do not show a distinct peak in this area (Fig. 8b).

3.3.2 Cu *K*-edge EXAFS

Cu *K*-edge EXAFS and the corresponding FT spectra are shown in Figure 9a and 9b.

The *k*-space data of surface, subsurface and deeply buried nodules (Fig. 9a) are significantly different, with a resonance at ~5.5 $Å^{-1}$ that decreases in intensity with burial depth. The FT spectra of all Cu *K*-edge EXAFS data have a peak at $R+\Delta R$ ~ 1.5 Å (Fig. 9b) that could be modeled with 3 to 4 O atoms at 1.96 Å (Table 2), using the model proposed by Peña et al. (2015). This implies that Cu is either in tetrahedral coordination or in octahedral-disordered configuration (see discussions in Sherman and Peacock, 2010; Manceau et al., 2014). The second distinct peak in the FT data, at $R+\Delta R \approx 2.45$ Å, corresponds to Cu-Mn distance, with a modelled distance for ~2 atoms at 2.87 to 2.88 Å and 1 atom at 3.42 to 3.45 Å in surface nodules (Table 2). These distances are compatible with Cu being incorporated at the edges of the phyllomanganate octahedra layers, within the plane formed by layer Mn (Peña et al., 2015), and with Cu in a TC configuration, respectively. From the ratio of the number of Mn atoms in each of these two shells, it is proposed that Cu incorporated in the layer is the main species for all samples whose EXAFS spectrum was modelled.

Subsurface and deeply buried nodules display a decrease of the amplitude of the Cu-Mn peak at $R+\Delta R \approx 2.45$ Å with burial depth. The decreasing of the amplitude generally corresponds to the decrease in the number of atomic neighbors, which is not clearly reflected in the data modeling. However, it was observed that the modelled Debye-Waller factors of this path increased, suggesting an increase in the degree of structural disorder in the Cu sites. However, since these two parameters (number of atomic neighbors and structural disorder) are often inversely correlated, this increase in structural disorder might also mask a decrease in the mean number of Mn neighbors in each Cu-Mn shell. Modeling of the buried nodules with the same structural model as the surface nodules was unsuccessful. Consequently, the Cu *K*-edge EXAFS were not modeled for subsurface and deeply buried nodules, as the results were found to be unreliable. However, the fact that the Cu *K*-edge EXAFS spectra of the buried nodules have a shape close to a sinusoidal curve, suggests the presence of a single shell around Cu, likely a Cu-O shell according to FT data (Fig. 9a).

3.3.3 Cobalt *K*-edge EXAFS

The mean Co *K*-edge EXAFS data of suboxic-diagenetic dendritic growth structures of a deeply buried nodule (22KL-801 cm) and the associated FT spectra are presented in Figure 10a and 10b and the modeling fit is summarized in Table 3. Similar to Ni and Cu *K*-EXAFS spectra, the Co *K*-EXAFS spectrum is composed of two main waves of differing frequencies (Fig. 10a), as evidenced by the two main peaks in the FT (Fig. 10b). The first peak in Fig. 10b corresponds to Co-O scattering ($R+\Delta R \approx 1.6$ Å) and the second peak to Co-Mn scattering ($R+\Delta R \approx 2.44$ Å; Manceau et al., 2014; Wu et al., 2019).

Modeling of the data resulted in the best fits with two different Co-O distances of 1.94 Å and 2.25 Å (see Table 3). However, the second peak only forms a small shoulder in the FT spectrum and is therefore only a minor component of the sample. The first distance is characteristic for Co^{3+}-O bonds and the second one is typical for Co^{2+}-O pair (e.g., Manceau et al., 1997). Furthermore, modelling of the first oxygen peak results in 6 oxygens, whereby only 2.6 oxygen neighbors can be modeled for Co^{2+}.

The second peak at R+ΔR=2.44 Å in FT (Fig. 10b) can be modeled with two Co-Mn bond distances at 2.88 Å and 3.08 Å (Table 3). The first Co-Mn distance is typical for Co^{3+} being incorporated within the octahedra sheets (^{E}Co), similar to Co incorporated in the octahedral layers of phyllomanganates (Manceau et al., 1997; Manceau et al., 2014; Wu et al., 2019). The second distance of 3.08 Å cannot be clearly assigned.

In contrast to previous studies, where Co is mainly incorporated into the vernadite phase of oxic-hydrogenetic LGS in surface nodules, Co in deeply buried nodules of this study is incorporated into the Mn-phase of the suboxic-diagenetic LGS, which is a tectomanganate such as todorokite according to the bulk XRD, IR measurements, and TEM analyses.

4. DISCUSSION

4.1 Mineralogy of buried nodules: transformation of phyllomanganate to todorokite and implications for the fate of metals

Surface and buried nodules have distinctly different mineralogical compositions due to the transformation of 10 Å phyllomanganate into todorokite that can be related to the burial process under oxic and suboxic conditions. Surface nodules are predominantly composed of Fe-vernadite and of 7 Å and 10 Å vernadite having a hexagonal layer symmetry (Wegorzewski and Kuhn, 2014; Wegorzewski et al., 2015). Todorokite is an accessory phase,

if present at all. In contrast, subsurface nodules (14-16 cm) are composed of both phyllomanganates and defective todorokite, whereby the latter is certainly an intermediate phase between phyllomanganate and tectomanganate (Bodeï et al., 2007). Nodules buried deep in the sediments (>530 cm) have todorokite as the major Mn-oxide phase. Heller et al., (2018) showed that Mn-nodules buried in suboxic deep-sea sediments are subject to diagenetic processes. These processes affect not only the chemical composition of the nodules and the surrounding sediments (Heller et al., 2018) but also their mineralogy. However, the exact transformation pathway from phyllomanganates to todorokite in the natural environment is still unclear (e.g., Atkins et al., 2014; 2016).

The synthetic route in the laboratory to produce todorokite begins with a *c*-ordered Mg-rich 10 Å phyllomanganate, which is subsequently exposed to high temperatures to transform into todorokite (~160°C; e.g., Bodeï et al., 2007). Different requirements are necessary for the phyllomanganate-to-tectomanganate transformation: **(I)** stacking of several MnO_2 sheets, **(II)** saturation of the interlayer with a cation capable of enforcing a ~10 Å layer-to-layer distance (e.g., Mg^{2+}) and **(III)** the presence of Jahn-Teller elements (e.g., Mn^{3+}, Cu^{2+}; Manceau et al., 2014; Bodeï et al., 2007, Grangeon et al., 2014). If any of these requirements is not fulfilled, the formation of tectomanganate from phyllomanganate is inhibited or incomplete (e.g., Bodeï et al., 2007).

In general, nodules from the sediment surface of the study area have been exposed during their growth history to alternately oxic and suboxic conditions (Wegorzewski and Kuhn, 2014; Kuhn et al., 2017b). As a result, hydrogenetic and suboxic-diagenetic LGS form. During oxic conditions, hydrogenetic LGS are formed due to metal (e.g. Mn, Fe, Co) precipitation from oxic seawater or oxic sediment pore water (Wegorzewski and Kuhn, 2014). Those LGS consist of vernadite, which is epitaxially intergrown with amorphous Fe-oxyhydroxides (δ-FeOOH) and has a Mn average oxidation state close to +4, which means low amounts of layer and interlayer Mn^{3+}. Moreover, vernadite contains a low amount of Cu^{2+} (0.34 ± 0.16wt.%; Wegorzewski and Kuhn, 2014) and therefore in general low amounts of Jahn-Teller elements (Mn^{3+}, Cu^{2+}). The Mg content of hydrogenetic LGS (0.3 – 3 wt.%) is lower than of suboxic-diagenetic LGS (1-4 wt.%). Furthermore, the internal, older parts of the surface nodules should predominantly consist of todorokite if this transformation would just be kinetically-controlled. However, the internal older parts of these nodules have the same alternating hydrogenetic and diagenetic LGS, as also observed in younger areas. According to

these results, we conclude that hydrogenetic vernadite is not able to transform to todorokite via early diagenetic processes under oxic conditions.

In contrast, under suboxic conditions within the sediments, Mn^{4+} can be reduced to aqueous Mn^{2+} that can be released into pore water and subsequently diffuses upward along concentration gradients until it is re-oxidized at the site of Mn nodule formation, contributing to diagenetic nodule growth. This process would lead to the formation of Mn-rich and Fe-poor suboxic-diagenetic LGS.

The nodule dissolution under suboxic conditions can be accompanied by Mn^{2+} readsorption by MnO_2 phases. In this case, Mn^{2+} will certaintly react with Mn^{4+} to produce Mn^{3+} (Elzinga, 2016; Grangeon et al., 2017), leading to an increased Mn^{3+}/Mn^{4+} ratio in the remaining nodule and thus favoring the phyllomanganates to todorokite transformation.

Concomitant with the reduction of the Mn-phase, associated elements such as Ni, Cu, and Co will be released in pore water where they will be available for incorporation in newly formed suboxic-diagenetic phyllomanganates having a Mn oxidation state lower than +4 and a Mg content to 4 wt.% (Wegorzewski and Kuhn, 2014). The presence of a Jahn-Teller cation (Mn^{3+}) and of an interlayer cation (Mg^{2+}) capable of enforcing a 10 Å layer-to-layer distance suggests that phyllomanganates of suboxic-diagenetic LGS have higher potential to transform to todorokite during early diagenesis than vernadite of hydrogenetic LGS from the same nodules. Therefore, we propose that if Mn-nodules become buried within suboxic sediments, 10 Å phyllomanganates of suboxic-diagenetic LGS will preferentially transform to todorokite over time. If nodules are exposed to suboxic conditions for a more extended period of time, the mineralogical transformations will likely be accelerated or intensified and therefore the crystal-chemistry of Ni, Cu and Co can be modified. More specifically, the hydrogenetic vernadite will continue to dissolve under suboxic conditions and Mn^{2+} together with its associated elements (Ni, Cu and especially Co) will be released into pore water (Manceau et al., 2014). This hypothesis explains the observation of Heller et al. (2018), who showed that deeply buried nodules have lower amounts of hydrogenetic LGS than surface nodules, and also that Ni, Cu and Co are enriched in pore waters around buried nodules. Furthermore, it is important to note that these buried nodules contain 40 % less Ni than nodules from the sediment surface (Heller et al., 2018).

Our data support the idea that the formation of todorokite from a 10 Å phyllomanganate precursor in marine nodules is predominantly a solid-state transformation as Bodeï et al. (2007) have proposed. As shown by Grangeon et al. (2014, 2015), Mn^{3+} located in the octahedral sheets can spontaneously migrate to interlayer sites to minimize steric strains

(steric strain results from a mismatch between the ideal geometry of an ion coordination sphere and the geometry of the crystallographic site of the ion) resulting from the Jahn-Teller distortion of the octahedral sheets, and contribute to the building of the "walls" of tectomanganates. The Jahn-Teller distortion is a geometric distortion of a nonlinear molecular system, which reduces its symmetry and energy. In an octahedral complex, two axial bonds are shorter/longer than the other four – (Chaudhary et al., 2015 and references therein). The same process may also affect Cu^{2+} initially incorporated in the layers of phyllomanganates, as well as the Mn^{3+} generated by interaction of the mineral surfaces with aqueous Mn^{2+}.

In contrast to our investigations, Elzinga (2011, 2016) showed that aqueous Mn^{2+} reacting with hexagonal birnessite at pH 7.5 causes reductive transformation of birnessite into Mn^{3+}-bearing Mn-phases such as feitknechite and manganite. If these Mn-phases are transformation products, they should be present as minor phases in the studied nodules. However, we were unable to detect these phases in our bulk XRD analyses. In our system, it is likely that the ratio of Mn^{2+} in solution to phyllomanganates was lower than that required to produce feitknechite or that the abundance of feitknechite was below 5% and as such was undetectable by bulk XRD. However, we cannot strictly rule out that, despite all cautions taken for sample preservation, traces of feitknechtite were initially present in the samples and were oxidized by atmospheric O_2 before sample analysis.

4.2 Crystal chemistry of trace metals (Ni, Cu, Co) and their behavior during mineralogical transformation

Ni^{2+} and Cu^{2+} can be incorporated into phyllomanganates (I) by adsorption above or below vacancy sites (forming a triple corner sharing complex: ^{TC}Me, where Me is the cation of interest), (II) by incorporation into a manganese layer sheet (^{E}Me), or (III) by adsorption at lateral edge surfaces (e.g., double corner sharing: ^{DC}Me; Manceau et al., 2014; Peacock et al., 2007a, b; Peña et al., 2015). In contrast, Co generally occurs as Co^{3+} incorporated within the octahedra sheets of phyllomanganates ($^{E}Co^{3+}$; Manceau et al., 2014).

The incorporation mechanism of these metals into tectomanganates such as todorokite is less documented (Manceau et al., 2014; Atkins et al., 2016; Wu et al., 2019). Mn^{4+} occupies the central and edge sites of the triple chains of todorokite tunnels while Mn^{3+}, Ni^{2+} and Cu^{2+} exclusively occupy the edge sites (Post and Bish, 1988; Bodeï et al., 2007, Manceau et al., 2014). Furthermore, metals such as Ni^{2+} can also form an outer-sphere complex in the todorokite tunnels (Pakarinen et al., 2010). To our knowledge, there are no data about the

location of Co into the todorokite structure of natural Mn-nodules. There are only few studies in the laboratory about the transformation of Co-bearing phyllomanganates into tectomanganates (Ching et al., 1999; Kumagai et al., 2005; Song et al., 2010; Wu et al., 2019). Co is generally enriched during hydrogenetic growth and is therefore incorporated into hydrogenetic vernadite rather than into suboxic-diagenetic Mn oxides.

In the following sections we will discuss the incorporation mechanism of Ni, Cu and Co in Mn-phases of deeply buried nodules in contrast to nodules from the sediment surface.

4.2.1 Nickel

Ni in surface nodules from this study is incorporated within the octahedra of the phyllomanganate sheets (^{E}Ni; Fig. 8b; Fig. 11a,b). In contrast, in deeply buried nodules (530cm – 987cm), Ni is mostly bound to todorokite. We propose that Ni preferentially occupies the middle sites of the triple octahedra chains (^{E}Ni) or the sites at the edges of the triple chains (^{TC}Ni; minor amount, Fig. 12a,b). With our assumption, Ni in todorokite of buried nodules can be expected to have fewer neighbors in the middle of the three octahedra than in phyllomanganates of surface nodules. This would explain the decrease of the R+ΔR ≈ 2.39 Å peak amplitude and furthermore the absence of a distinct peak at R+ΔR ≈ 3.2 Å in the FT Ni-EXAFS spectra (Fig. 8b). However, an alternative explanation for the decrease of the ^{E}Ni peak at R+ΔR ≈ 2.39 Å and the absence of a distinct peak for Ni in the octahedra triple chains of todorokite would be that Ni could be present in a disordered environment or that a part of the Ni forms an outer-sphere complex in the tunnels of todorokite (Fig. 12b; Pakarinen et al., 2010). Atkins et al., (2016) showed that during the transformation of a synthetic Ni-bearing phyllomanganate into todorokite, up to 50 % of the Ni was released, which is similar to what we observe here. As noted above in section 4.1, nodules from the sediment surface consist of phyllomanganates and contain 40 % more Ni than the deeply buried nodules, which consist mainly of todorokite (Wegorzewski and Kuhn, 2014; Wegorzewski et al., 2015; Heller et al., 2018). Furthermore, sample 22KL-801cm shows a modeled Ni-Mn distance of 4, which cannot be attributed to ^{E}Ni incorporation in phyllomanganates or todorokite. Our Ni-EXAFS analysis of buried nodules indicates that Ni is released in solution during the phyllomanganate-to-tectomanganate transformation.

4.2.2 Copper

According to Heller et al. (2018), Cu concentration in nodules from the sediment surface and those buried are similar. In contrast to Ni^{2+}, Cu^{2+} favors the transformation from

phyllomanganates into tectomanganates and may remain in the structure during this transformation (Burns and Burns 1978; Usui, 1979; Atkins et al., 2016).

Modeling Cu-EXAFS of surface nodules with the model of Peña et al. (2015) shows that Cu is preferentially incorporated as ^{E}Cu, similar to Ni, but with fewer atomic neighbors resulting in a lower amplitude of the ^{E}Cu-Mn peak compared to the ^{E}Ni-Mn peak (Fig. 11a). These results may be interpreted in terms of the Cu in surface nodules being preferentially located at the edges of the phyllomanganate sheets with only 3 to 4 atomic neighbors (Fig. 11b; Peña et al., 2015). In all nodules, ^{TC}Cu is present in low amounts, as witnessed by the low intensity of the correlation at R+ΔR≈3.2 Å in the FT and by data modeling (Fig. 9b, 11a; Table 2).

In contrast to surface nodules, Cu-EXAFS data of the deeply buried nodules show a sinusoidal curve in the *k*-space, which suggests only one coordination shell (Fig. 9a). The FT data of these Cu-EXAFS data have only one distinct peak around R+ΔR ≈ 1.5 Å suggesting that O is the only neighbor of Cu compared to FT Ni-EXAFS data of deeply buried nodules (Fig. 8; 12). These results suggest that Cu is bound as an outer-sphere complex in todorokite of deeply buried nodules (Fig. 12b), as previously assumed for Ni (Pakarinen et al., 2010). Another explanation could be that Cu is increasingly bound in a disordered configuration to one or more sorption site(s) with increasing depth of burial.

Furthermore, we compared the Cu-EXAFS data of bulk nodules of this study with Cu-EXAFS analyses of Manceau et al. (2014) (Fig. 13). The authors recorded Cu-EXAFS of a phyllomanganate-rich area, a todorokite-rich area, and a clay-rich area in a natural Mn nodule from the Pacific Ocean. The Cu-EXAFS of surface nodules from this study (phyllomanganate-rich) are similar to Cu-EXAFS of the todorokite-rich region (CuD465D2) of Manceau et al. (2014). In contrast, Cu-EXAFS analyses of subsurface nodules of this study (phyllomanganates and todorokite/defective todorokite) match well with Cu-EXAFS of the phyllomanganate-rich region of the surface nodule (CuD465D1; Manceau et al., 2014; Fig. 13).

One could expect that, as nodules from the sediment surface become buried and thus as phyllomanganates transform to todorokite, Cu remains in the crystal structure of the Mn oxides. This would produce a spectrum for buried nodules that would be close to that reported by Manceau et al. (2014; CuD465D2), with a dominant peak at 3.5 Å, which is not the case (Fig. 9a, b). We speculate that Cu underwent an additional step with regards to the aforementioned mechanisms; after it Cu was incorporated within the Mn sites at the edges of the triple chains of todorokite (Post and Bish, 1988; Post et al., 2003; Bodaï et al., 2007; Manceau et al., 2014), but subsequently migrated out of the structure after the nodules were

562 subject to suboxic conditions for a longer period of time (Fig. 12b). If nodules become
563 exposed to suboxic conditions for a long period of time, not only vernadite of hydrogenetic
564 LGS dissolves, but the 7 Å and 10 Å phyllomanganates as well as todorokite will also begin
565 to dissolve. In the course of the Mn dissolution, Cu will be released from Mn octahedra,
566 migrate into the tunnels or at the todorokite surface, or adsorb to another phase, and would in
567 all cases form an outer-sphere complex before being ultimately released into the pore water.
568 Coherently, the Cu-EXAFS spectrum of deeply buried Mn-nodules agrees well with that of
569 clay-rich regions (smectite-rich; CuD465DH; Manceau et al., 2014. Fig. 13a,b). According to
570 a number of authors (Boström et al., 1974; Manceau et al., 2014), Cu may also be associated
571 with organic matter, biogenic silica, phosphates, carbonates or aluminosilicates that may also
572 show FT data of Cu-EXAFS with sinusoidal curves and only one distinct peak around
573 R+ΔR~1.5 Å. However, our statistical analyses, individual high resolution measurements
574 using electron microprobe, as well as leaching experiments of surface and buried nodules, all
575 suggest that Cu is strongly associated with Mn oxides and to a lesser degree with Fe
576 oxyhydroxides and not with other phases in the Mn-nodules (e.g., Mohwinkel et al., 2014;
577 Wegorzewski and Kuhn, 2014; Heller et al., 2018). Further work would be required to explain
578 this potential discrepancy, and discriminate between a difference in sorption site and in an
579 intimate association of different minerals (e.g., Mn oxides and a minor amount of clays) that
580 would thus be hardly distinguishable with the method used here. Note however that the
581 presence of Cu bound to organic matter is unlikely, as the total organic carbon content of the
582 present samples is ≤ 0.05%.
583
584 **4.2.3 Cobalt**
585 The enrichment of Co in the suboxic-diagenetic LGS of Mn-nodules from the CCZ is unusual
586 because Co is typically enriched in oxic-hydrogenetic vernadite due to oxidative scavenging
587 on Mn-oxides (Kuhn et al., 2017a), following well documented mechanisms (e.g., Koschinsky
588 and Halbach, 1995; Byrne, 2002; Manceau et al., 1997; 2014).
589 Our Co *K*-EXAFS analyses show that Co is predominantly incorporated as $^{E}Co^{3+}$ in the
590 phyllomanganates while, in the case of todorokite, it would be incorporated at a Mn site
591 located in the Mn row that is not adjacent to a "wall", because no correlation ~3.4 Å
592 (Manceau et al., 1997; Fig. 12b) could be observed in the FT. Our Co-EXAFS data are similar
593 to those from a hydrogenetic area (D465H) in a nodule examined by Manceau et al. (2014) in
594 which all Co is incorporated into vernadite. According to our EPMA maps of the buried

nodule, Co is highly enriched (1.2 wt.%; Heller et al., 2018) in the suboxic-diagenetic dendritic LGS, which are made up of "defective todorokite"/todorokite instead of vernadite.

Based on the presence of a second Co-O distance, a small proportion of Co occurs as Co^{2+}. The modeled Co-Mn distance of 3.08 Å was attributed to this Co^{2+}, since it is too short for Co^{3+} sharing corners with Mn octahedral in todorokite, or for surface adsorption of Co at triple corner and/or edge sites on layered Mn oxides (^{Tc}Co; Manceau et al., 1997; Wu et al., 2019).

Asbolane was not detected in the bulk analysis of deeply buried nodules; therefore we speculate that CoOOH is not present in our samples.

However, the high enrichment of Co in suboxic-diagenetic LGS is uncommon and may be explained by secondary enrichment processes. Over time, as buried Mn-nodules become exposed to suboxic environmental conditions, vernadite of hydrogenetic LGS starts to dissolve, whereas the 10 Å phyllomanganates of diagenetic LGS remain stable. During dissolution of vernadite the Mn-associated elements Ni, Cu, and especially Co will be released into pore water (as Co^{2+}) and are available for further re-incorporation into the more stable Mn-phases such as 10 Å phyllomanganates or newly formed todorokite. It is interesting to note that only Co is significantly enriched in those phases and not Ni or Cu. A possible mechanism might be a redox coupling of dissolved Co^{2+} with solid-phase Mn^{4+}, where Co^{2+} is oxidized to Co^{3+} and Mn^{4+} is reduced to soluble Mn^{2+} (Heller et al., 2018). The similar ionic radius of Co^{3+} and Mn^{4+} (0.53 Å versus 0.54 Å) allows Co^{3+} to substitute for Mn^{4+} in the middle of the octahedral chains of todorokite after the transformation of phyllomanganates to todorokite (Fig. 12).

The occurrence of minor amounts of Co^{2+} in the deeply buried nodules can arise from: (i) Co^{2+} that remains adsorbed at edges of the Mn octahedra sheets or (ii) Co^{2+}-hydroxides that form in the interlayer of defective todorokite structures (cf asbolane); or (iii) Co^{2+} formed by reduction of Co^{3+} recently released from dissolving Mn-phases (together with Ni and Cu). The latter hypothesis is supported by an increase of Co^{2+} concentration in pore water in the sediment depth around the deeply buried nodules (Heller et al., 2018).

4.3 Location of nodule formation

In the discussion provided above we suggest that all buried nodules of this study primarily formed at the sediment surface and were subsequently buried within the sediment column. We do not think that the buried nodules were formed in situ within the sediments as a sedimentary layer.

This is because: (1) The shape and morphology, as well as the internal growth structures (hydrogenetic and suboxic-diagenetic LGS), are very similar to surface nodules (Halbach et al., 1988; Wegorzewski and Kuhn, 2014). (2) The buried nodules clearly show signs of dissolution such as a grainy surface, brittle appearance and dissolved internal layers (Heller et al., 2018). (3) Diagenetic Mn-oxide formation in deep sea sediments would form continuous layers rather than single, individual nodules (Thomson et al., 1987; Jarvis and Higgs, 1987). (4) In this area, Mn-nodules can become buried within the sediment due to increased sedimentation rates (von Stackelberg 1997). (5) In general the formation of all Mn-nodules needs the presence of an oxic/suboxic front at the position of nodule formation. Only the sediment surface provides stable conditions over a long period of time for the presence of such a front. In contrast, within the sediments the location of this front moves up and down due to varying sedimentation conditions (sedimentation rates, flux of organic material). (6) The current oxic/suboxic front within the sediment column of the working area is located at 2-3 m sediment depth (Mewes et al., 2014). We have not found Mn-nodules at this front in any of these cores (Kuhn et al., 2015; Heller et al., 2018; Mewes et al., 2014). Mn-nodules were either found below or above this front.

5. SUMMARY AND CONCLUSIONS

This study identifies the processes that occur during mineral transformation of Mn oxide phases of Mn-nodules under suboxic conditions in the deep-sea sedimentary environment, and how those transformations influence the distribution of Ni, Cu, and Co. Mn-nodules from the sediment surface are typically mixed-type nodules consisting of hydrogenetic and suboxic-diagenetic LGS. Hydrogenetic LGS consist of vernadite and amorphous FeOOH, and the suboxic-diagenetic LGS consist of 7 Å and 10 Å phyllomanganates. From EXAFS data, Ni in surface nodules is incorporated at random sites of the manganese layer sheets with up to 6 atomic neighbors, whereas Cu is preferentially incorporated at the edges of the phyllomanganate sheets with lower amount of atomic neighbors.

In subsurface nodules, phyllomanganates start to transform to tectomanganates, but Cu, Ni and Co remain incorporated within the octahedral Mn oxide sheets.

In contrast, the deeply buried nodules (>530 cm) predominantly consist of tectomanganates such as todorokite. Nickel in deeply buried nodules is primarily incorporated as ^{E}Ni in the middle of the octahedra chains forming the todorokite tunnels and probably partly being bound as outer-sphere complexes within the todorokite tunnels. In contrast, Cu in deeply buried nodules appears to be completely bound as outer-sphere complexes within the

663 todorokite tunnels. Like Ni, Co appears to be incorporated mainly in the middle of octahedral
664 chains of todorokite in deeply buried nodules.
665 In general, all of the Mn-nodules, independent of their location in the sediment column, are or
666 were mixed type nodules consisting of hydrogenetic as well as suboxic-diagenetic LGS.
667 Subsurface and deeply buried nodules likely formed at the sediment surface, and were
668 subsequently buried due to a change in sedimentation rate or other geological events. Since
669 sub-surface nodules are older than surface nodules (unpublished BGR data), they have been
670 subject to suboxic diagenetic processes over a longer period of time which may have
671 promoted the transformation of phyllomanganates to tectomanganates.
672 However, if mixed type nodules are buried at depth with prolonged suboxic conditions, then
673 Mn oxide phases start to dissolve. At the beginning of the dissolution only vernadite of
674 hydrogenetic LGS dissolve, releasing Mn^{2+} and associated metals such as Co^{2+} into pore
675 waters. Dissolved Mn^{2+} can react with the more stable 7 Å and 10 Å phyllomanganates and
676 transforms them into tectomanganates such as todorokite. Furthermore, the released Co^{2+} can
677 be re-adsorbed on the more stable Mn oxide phase (in this case "defective
678 todorokite"/todorokite) and will be incorporated into the octahedral structure of the
679 tectomanganates due to a redox-reaction with Mn^{4+} and/or Mn^{3+}. If these nodules remain
680 under such suboxic conditions, the more ordered Mn-phases such as todorokite will also start
681 to dissolve and only the Fe-phases (δ-FeOOH/Fe_2O_3) will eventually remain. Furthermore,
682 during the Mn-oxide dissolution, Ni and Cu start to migrate from the octahedra sheets into the
683 tunnels or above the sheets and will be adsorbed as outer-sphere complexes before being
684 completely released into the sediment pore waters.
685
686 **ACKNOWLEDGEMENTS**
687 We greatly appreciate the work of the master and his crew on expeditions SO205 and SO240
688 with R/V Sonne during which the samples for this study were taken.
689 We thank C. Wöhrl and S. Goldmann for an excellent support during the EMP analysis at the
690 Federal Institute for Geosciences and Natural Resources (BGR). We also thank M. Hein
691 (BGR) for conducting the IR-spectroscopy and S. Kaufhold (BGR) for discussing the IR
692 results. Furthermore, we gratefully acknowledge the expert help of Mrs. A. Schreiber from the
693 GFZ in Potsdam for foil preparation using FIB and Dr. Fabienne Warmont for the HRTEM
694 analyses. This work was funded as internal BGR project (Project: MeMa: A-0203008.A) and
695 by the German Federal Ministry for Education and Research (BMBF) under the grant
696 03G0240A. S. Grangeon acknowledges funding by the French National Research Agency

(ANR, grant ANR-14-CE01-0006) and by a BRGM project. Furthermore, we gratefully thank the beam line scientist R. Davis (beam line 4-1) at the SSRL for helping during the EXAFS measurements. Use of the Stanford Synchrotron Radiation Lightsource, SLAC National Accelerator Laboratory, is supported by the U.S. Department of Energy, Office of Science, and Office of Basic Energy Sciences under Contract No. DE-AC02-76SF00515. The SSRL Structural Molecular Biology Program is supported by the DOE Office of Biological and Environmental Research, and by the National Institutes of Health, National Institute of General Medical Sciences (including P41GM103393). The contents of this publication are solely the responsibility of the authors and do not necessarily represent the official views of NIGMS or NIH.

REFERENCES

Atkins, A.L., Shaw, S. and Peacock, C.L. (2014) Nucleation and growth of todorokite from birnessite: Implications for trace-metal cycling in marine sediments. Geochim. Cosmochim. Acta **144**, 109-125.

Atkins, A.L., Shaw, S. and Peacock, C.L. (2016) Release of Ni from birnessite during transformation of birnessite to todorokite: Implications for Ni cycling in marine sediments. Geochim. Cosmochim. Acta **189**, 158 – 183.

Banerjee, R., Iyer, S.D. and Dutta, P. (1991) Buried nodules and associated sediments from the Central Indian Basin. Geo-Mar Lett **11**, 103-107.

Blöthe, M., Wegorzewski, A.V., Müller, C., Simon, F., Kuhn, T. and Schippers, A. (2015) Manganese-Cycling Microbial Communities Inside Deep-Sea Manganese Nodules. Environ. Sci. Technol. **49**, 7692-7700.

Bodeï, S., Manceau, A., Geoffroy, N., Baronnet, A., Buatier, M. (2007) Formation of todorokite from vernadite in Ni-rich hemipelagic sediments. Geochim. Cosmochim. Acta **71**, 5698–5716.

Boström, K., Joensuu, O. and Brohm, I. (1974) Plankton: Its chemical composition and its significance as a source of pelagic sediments. Chem. Geol. **14**, 255–271.

Burns R.G. and Burns V.M. (1977) Mineralogy of ferromanganese nodules. Marine Manganese Deposits (ed. G.P. Glasby). Elsevier, Amsterdam.

727 Burns, V.M. and Burns, R.G. (1978) Authigenic todorokite and phillipsite inside deep-sea
728 manganese nodules. Am. Mineral. **63**, 827–831.

729 Byrne R.H., (2002). Inorganic speciation of dissolved elements in seawater: the influence of
730 pH on concentration ratios. Geochem. Trans., **2**, 11-16.

731 Chaudhary, T., Khamar, J., Chaudhary, P., Chaudhary, V., Barot, M., & Sen, D. J. (2015).
732 Jahn–Teller distortions: a new strategy in quantum mechanics. J Drug Discov Therap. **3**, 09-
733 16.

734 Ching, S., Krukowska, K.S. and Suib, S.L. (1999). A new synthetic route to todorokite-type
735 manganese oxides. Inorg. Chim. Acta **294**, 123-132.

736 Cronan, D.S. and Tooms, J.S. (1967) Sub-surface concentrations of manganese nodules in
737 Pacific sediments. Deep Sea Res. **14**, 117-119.

738 Davison, W. (1993) Iron and manganese in lakes. Earth-Sci. Rev **34**, 119-163.

739 Drits, V.A., Silvester, E., Gorshkov, A.I. and Manceau, A. (1997) Structure of synthetic
740 monoclinic Na-rich birnessite and hexagonal birnessite: I. Results from X-ray diffraction and
741 selected-area electron diffraction, Am. Mineral. **82**, 946–961.

742 Drits, V.A., Lanson, B. and Gaillot, A.C. (2007). Birnessite polytype systematics and
743 identification by powder X-ray diffraction. Am. Mineral., **92**, 771-788.

744 Elzinga, E.J. (2011). Reductive transformation of birnessite by aqueous Mn (II). Environ. Sci.
745 Technol, **45**, 6366-6372.

746 Elzinga, E. J. (2016). ^{54}Mn radiotracers demonstrate continuous dissolution and
747 reprecipitation of vernadite (δ-MnO_2) during interaction with aqueous Mn (II). Environ. Sci.
748 Technol, **50**, 8670-8677.

749 Giannuzzi, L.A., and Stevie, F.A. (2005) Introduction to Focused Ion Beams: Instrumentation,
750 Theory, Techniques and Practice, 98 p. Springer, Berlin.

751 Giannuzzi, L.A., Drown, J.L., Brown, S.R., Irwin, R.B. and Stevie, F.A. (1997) Focused ion
752 beam milling and micromanipulation lift-out for site-specific cross-section TEM specimen
753 preparation. In R. Anderson and S. Walck, Eds., Proceedings of the Materials Research
754 Society: Workshop on Specimen Preparation for TEM of Materials IV, 480. Materials
755 Research Society, Pittsburgh, Pennsylvania, p. 19–27.

Golden, D.C., Dixon, J.B. and Chen, C.C. (1986) Ion exchange, thermal transformations, and oxidizing properties of birnessite. Clays Clay Miner. **34**, 511–520.

Grangeon, S., Fernandez-Martinez, A., Warmont, F., Gloter, A., Marty, N., Poulain, A. and Lanson, B. (2015). Cryptomelane formation from nanocrystalline vernadite precursor: a high energy X-ray scattering and transmission electron microscopy perspective on reaction mechanisms. Geoch. Trans., **16**, 12.

Grangeon, S., Lanson, B. and Lanson, M. (2014) Solid-state transformation of nanocrystalline phyllomanganate into tectomanganate: influence of initial layer and interlayer structure. Acta Crystallographica Section B: Structural Science, Cryst. Res. Technol. **70**, 828-838.

Grangeon, S., Warmont, F., Tournassat, C., Lanson, B., Lanson, M., Elkaïm, E. and Claret, F. (2017). Nucleation and growth of feitknechtite from nanocrystalline vernadite precursor. Eur J Mineral, **29**, 767-776.

Halbach, P., Friedrich, G., von Stackelberg, U., 1988. The Manganese Nodule Belt of the Pacific Ocean. Geological Environment, Nodule Formation, and Mining Aspects. Ferdinand Enke Verlag, Stuttgart, pp. 254

Haeckel, M., König, I., Riech, V., Weber, M. E. and Suess, E. (2001). Pore water profiles and numerical modelling of biogeochemical processes in Peru Basin deep-sea sediments. Deep Sea Research Part II: Topical Studies in Oceanography, **48**, 3713-3736.

Hein, J.R., Mizell, K., Koschinsky, A. and Conrad, T.A. (2013) Deep-ocean mineral deposits as a source of critical metals for high- and green-technology applications: Comparisons with land-based resources. Ore Geol. Rev. **51**, 1-14.

Heller, C., Kuhn, T., Versteegh, G.J.M., Wegorzewski, A.V., and Kasten, S. (2018). The geochemical behavior of metals during alteration of manganese nodules buried in deep-sea sediments. Deep Sea Res. Part I: Oceanographic Research Papers,

Heye, D., Marchig, V. and Meyer, H. (1979). The growth of burial manganese nodules. Deep Sea Res. **26A**, 789-798.

Jarvis, I., Higgs, N. (1987): Trace-element mobility during early diagenesis in distal turbidites: late Quaternary of the Madeira Abyssal Plain, N Atlantic. In: P.P.E. Weaver, J. Thompson (eds). Geology and Geochemistry of Abyssal Plains. Geological Society Special Publications **31**, pp. 179-213.

786 Julien, C. M., Massot, M. and Poinsignon, C. (2004) Lattice vibrations of manganese oxides:
787 Part I. Periodic structures. Spectrochim. Acta A: Molecular and Biomolecular Spectroscopy
788 **60**, 689-700.

789 Kang, L., Zhang, M., Liu, Z. H., and Ooi, K. (2007). IR spectra of manganese oxides with
790 either layered or tunnel structures. Spectrochim. Acta A: Molecular and Biomolecular
791 Spectroscopy **67**, 864-869.

792 Koschinsky, A. and Halbach, P. (1995) Sequential leaching of marine ferromanganese
793 precipitates: genetic implications. Geochim. Cosmochim. Acta **59**, 5113–5132.

794 Koschinsky, A. and Hein, J. R. (2003). Uptake of elements from seawater by ferromanganese
795 crusts: solid-phase associations and seawater speciation. Mar. Geol., **198**, 331-351.

796 Koschinsky, A., and Hein, J. R. (2017). Marine ferromanganese encrustations: Archives of
797 changing oceans. Elements: An International Magazine of Mineralogy, Geochemistry, and
798 Petrology, **13**, 177-182.

799 Kuhn, T. and Shipboard Scientific Party (2015) Low-temperature fluid circulation at
800 seamounts and hydrothermal pits: Heat flow regime, impact on biogeochemical processes and
801 its potential influence on the occurrence and composition of manganese nodules in the NE
802 Pacific, Cruise Report SO240/FLUM: Hannover, Germany, 185 p.

803 Kuhn, T., Wegorzewski, A., Rühlemann, C., Vink, A. (2017a) Composition, formation, and
804 occurrence of polymetallic nodules. In: Sharma, R., (eds.). Deep-Sea Mining. Springer,
805 Cham, pp. 23-63.

806 Kuhn, T., Versteegh, G.J.M., Villinger, H., Dohrmann, I., Heller, C., Koschinsky, A., Kaul,
807 N., Ritter, S., Wegorzewski, A.V. and Kasten, S. (2017b) Widespread seawater circulation in
808 18–22 Ma oceanic crust: Impact on heat flow and sediment geochemistry. Geol. **45**, 799-802.

809 Kumagai, N., Komaba S., Abe, K. and Yashiro, H. (2005). Synthesis of metal-doped
810 todorokite-type MnO2 and its cathode characteristics for rechargeable lithium batteries. J.
811 Power Sources **146**, 310-314.

812 Lynn, D. C. and Bonatti, E. (1965) Mobility of manganese in diagenesis of deep-sea
813 sediments. Mar. Geol. **3**, 457-474.

814 Manceau, A., Lanson, M. and Geoffroy, N. (2007) Natural speciation of Ni, Zn, Ba and As in
815 ferromanganese coatings on quartz using X-ray fluorescence, absorption and diffraction.
816 Geochim. Cosmochim. Acta **71**, 95–128.

817 Manceau, A., Lanson, M. and Takahashi, Y. (2014) Mineralogy and crystal chemistry of Mn,
818 Fe, Co, Ni, and Cu in a deep-sea Pacific polymetallic nodule. Am. Mineral. **99**, 2068-2083.

819 Manceau, A., Drits, V.A., Silvester, E., Bartoli, C., and Lanson, B. (1997) Structural
820 mechanism of Co^{2+} oxidation by the phyllomanganate buserite. Am. Mineral., **82**, 1150–1175.

821 Moore, W.S. (1981) Iron-manganese banding in Oneida Lake ferromanganese nodules. Nat.
822 **292**, 233-235.

823 Mohwinkel, D., Kleint, C. and Koschinsky, A. (2014). Phase associations and potential
824 selective extraction methods for selected high-tech metals from ferromanganese nodules and
825 crusts with siderophores. Appl. Geochem. **43**, 13-21.

826 Pakarinen, J., Koivula, R., Laatikainen, M., Laatikainen, K., Paatero, E. and Harjula, R.
827 (2010) Nanoporous manganese oxides as environmental protective materials—Effect of Ca
828 and Mg on metals sorption. J. Hazard. Mater. **180**, 234-240.

829 Pal'chik, N.A., Grigor'eva, T.N. and Moroz, T.N. (2011) Natural and synthetic manganese
830 minerals. Russ. J. Inorg. Chem. **58**, 138–143.

831 Pattan, J.N. and Parthiban, G. (2007). Do manganese nodules grow or dissolve after burial?
832 Results from the Central Indian Ocean Basin. J. Asian Earth Sci. **30**, 696-705.

833 Peacock, C.L. (2009): Physiochemical controls on the crystal-chemistry of Ni in birnessite:
834 Genetic implications for ferromanganese precipitates. Geochim. Cosmochim. Acta **73**, 3568 –
835 3578.

836 Peacock, C.L. and Sherman, D.M. (2007a) Sorption of Ni by birnessite: Equilibrium controls
837 on Ni in seawater. Chem. Geol. **238**, 94 – 106.

838 Peacock, C.L. and Sherman, D.M. (2007b) Crystal-chemistry of Ni in marine ferromanganese
839 crusts and nodules. Am. Mineral. **92**, 1087 – 1092.

840 Peña, J., Bargar, J. R. and Sposito, G. (2015). Copper sorption by the edge surfaces of
841 synthetic birnessite nanoparticles. Chem. Geol. **396**, 196-207.

842 Potter, R.M. and Rossman, G.R. (1979) The tetravalent manganese oxides: identification,
843 hydration, and structural relationships by infrared spectroscopy. Am. Mineral. **64**, I199-1218.

844 Post, J.E. and Bish, D.L. (1988) Rietveld refinement of the todorokite structure. Am. Mineral.
845 **73**, 861–869.

846 Ravel, B. and Newville M. (2005) ATHENA, ARTEMIS, HEPHAESTUS: data analysis for
847 X-ray absorption spectroscopy using IFEFFIT. J SYNCHROTRON RADIAT 4, 537-541.

848 Rühlemann, C., Kuhn, T., Wiedicke, M., Kasten, S., Mewes, K. and Picard, A. (2011) Current
849 status of manganese nodule exploration in the German license area. In Ninth ISOPE Ocean
850 Mining Symposium. International Society of Offshore and Polar Engineers.

851 Rühlemann, C. and Shipboard Scientific Party (2018). MANGAN 2018 Cruise Report:
852 Geology, Biodiversity and Environment of the German License Area for the Exploration of
853 Polymetallic Nodules in the Equatorial NE Pacific, Guayaquil, Ecuador – Suva, Fiji, 6th April
854 – 29th May 2018, February 2019, Bundesanstalt für Geowissenschaften und Rohstoffe
855 (BGR), Hannover, Germany.

856 Sherman, D.M. and Peacock, C.L. (2010) Surface complexation of Cu on birnessite (δ-
857 MnO_2): Controls on Cu in the deep ocean. Geochim. et Cosmochim. Acta **74**, 6721 – 6730.

858 Song, C., Li, R., Liu, F., Feng, X., Tan, W. and Qiu, G. (2010). Cabalt-doped todorokites
859 prepared by refluxing at atmospheric pressure as cathode materials for Li batteries.
860 Electrochim. Acta **55**, 9157-9165.

861 Tazaki, K. (2000). Formation of banded iron-manganese structures by natural microbial
862 communities. Clays Clay Miner. **48**, 511-520.

863 Thomson, J., Colley, S., Higgs, N.C., Hydes, D.J., Wilson, T.R.S., Sorensen, J. (1987).
864 Geochemical oxidation fronts in NE Atlantic distal turbidites and their effects in the
865 sedimentary record. In: P.P.E. Weaver, J. Thompson (eds). Geology and Geochemistry of
866 Abyssal Plains. Geological Society Special Publications 31, pp. 167-177.

867 Uspenskaya, T.Y.,Gorshkov, A.I. and Sivtsov, A.V. (1987) Mineralogy and internal structure
868 of Fe-Mn-nodules from the Clarion-Clipperton fracture zone. Int. Geol. Rev. **29**, 363–371.

869 Usui, A., and Terashima, S. (1997). Deposition of hydrogenetic and hydrothermal manganese
870 minerals in the Ogasawara (Bonin) arc area, northwest Pacific. Mar. Geores. and Geotech. **15**,
871 127-154.

872 Usui, A. (1979) Minerals, metal contents, and mechanism of formation of manganese nodules
873 from the central Pacific basin (GH76-1 and GH77-1 Areas). Mar. Geol. Oceanography of the
874 Pacific manganese nodule province, pp.651-679.

875 Villalobos, M., Toner, B., Bargar, J., and Sposito, G. (2003) Characterization of the
876 manganese oxide produced by Pseudomonas putida strain MnB1. Geochim. Cosmochim. Acta
877 **67**, 2649–2662.

878 Von Stackelberg, U., (1997) Growth history of manganese nodules and crusts of the Peru
879 Basin. Geological Society, London, Special Publications, 119, pp.153-176.

880 Wegorzewski, A.V. and Kuhn, T. (2014) The influence of suboxic diagenesis on the
881 formation of manganese nodules in the Clarion Clipperton nodule belt of the Pacific Ocean.
882 Mar. Geol. **357**, 123-138.

883 Wegorzewski, A.V., Kuhn, T., Dohrmann, R., Wirth, R. and Grangeon S. (2015)
884 Mineralogical characterization of individual growth structures of Mn-Nodules with different
885 Ni+Cu content from central Pacific Ocean. Am. Mineral. **100**, 2497-2508.

886 Wirth, R. (2004) Focused Ion Beam (FIB): a novel technology for advanced application of
887 micro-and nanoanalysis in geosciences and applied mineralogy. Eur. J. Mineral. **16**, 863–876.

888 Wirth, R. (2009) Focused Ion Beam (FIB) combined with SEM and TEM: Advanced
889 analytical tools for studies of chemical composition, microstructure and crystal structure in
890 geomaterials on a nanometre scale. Chemi. Geol. **261**, 217–229.

891 Wu, Z., Peacock, C.L., Lanson, B., Yin, H., Zheng, L., Chen, Z., Tan, W., Qiu, G., Liu, F.,
892 Feng, X. (2019) Transformation of Co-containing birnessite to todorokite: Effect of Co on the
893 transformation and implications for Co mobility. Geochim. Cosmochim. Acta **246**, 21-40.

Figure captions:

Figure 1: Bathymetric map of the eastern German contract area with locations of nodules studied here (from Kuhn et al., 2015).

Figure 2 a: Backscattered electron (BSE) map of individual layer growth structures (LGS) of a Mn nodule from the sediment surface (SO205-32KG, 3µm beam size). **b-f:** Element distribution maps of individual LGS of the surface nodule shown in a. Based on Mn and Fe, two distinct LGS can be recognized: Mn-rich LGS of suboxic origin and Fe-rich LGS of hydrogenetic origin. Copper and Ni are more strongly enriched than Co in the Mn-rich LGS. Cobalt is more highly enriched in Fe-rich areas.

Figure 3 a: Backscattered electron (BSE) map of layer growth structures (LGS) of a deeply buried Mn nodule (SO240-22KL-801cm, 5 µm beam size). The red square marks the magnification of the Fe-rich LGS in figure 4. **b-f:** Element distribution maps of individual LGS of the deeply buried Mn nodule shown in a. Here Mn and Fe are well fractionated. The Fe-rich LGS is completely depleted in metals (e.g., Ni, Cu, Co). Metals are associated with Mn at the rims of the suboxic-diagenetic dendritic LGS. Co is also enriched to suboxic-diagenetic LGS.

Figure 4: BSE image magnification of the red square area in figure 3a. The Fe-rich LGS is not homogenous but rather a mixture of remaining hydrogenetic material that is in a different state of dissolution than the suboxic-diagenetic LGS and the newly formed Fe-rich phases.

Figure 5: XRD patterns of Mn nodules from the sediment surface (21KG) compared with nodules which are buried in shallow (subsurface: 14 – 16 cm) and deep sediment (>530 cm). All nodules were analyzed after drying at 40°C (black pattern) and 105°C (grey pattern) causing the differences in the diffraction pattern at the same intensity level. Stars (*) indicate other minerals such as feldspar, quartz and phillipsite.

Figure 6 a: High Resolution Transmission Electron Microprobe (HRTEM) image of the dendritic growth structure close to the Fe-Si-Al LGS area, where the foil comes from is marked as a red square in figure 3a. **b:** HRTEM image of dendritic LGS within buried nodule 22KL-801cm. Different mineral phases can be recognized such as phyllomanganates and tectomanganates.

Figure 7: IR spectra of three surface nodules, two subsurface nodules and four deeply buried nodules, from 2200 to 400 wavenumbers [cm^{-1}]. The arrows mark the IR bands that are characteristic for manganate oxides (phyllomanganate and todorokite). Deeply buried nodules show an additional broad band at ~760 cm^{-1} that is typical for tunnel manganese oxides (todorokite) and is absent in surface nodules.

Figure 8: Ni *K*-edge EXAFS spectra (a) and their respective Fourier transformed (FT) EXAFS measurements (b) of surface, subsurface and deeply buried nodules. The peaks indicated by the arrows between 6 and 7 k $Å^{-1}$ (a) show the changes between surface and deeply buried nodules.

Figure 9: Cu *K*-edge EXAFS spectra (a) and their respective Fourier transformed (FT) EXAFS measurements (b) of surface, subsurface, and deeply buried nodules. The arrows between 5 and 6 k $Å^{-1}$ (a) mark the changes between surface and deeply buried nodules. Deep buried nodules only show one oscillation, which is the first shell around the Cu atom (oxygen; Cu-O binding). **b:** The intensity of the peak around 2.45 Å (Cu-Mn) decreases with increasing sediment depth where nodules were buried.

Figure 10: Co *K*-edge EXAFS spectrum (**a)** and Co Fourier transformed (FT) EXAFS measurement (**b**) (data show a merge of different measurements) on Co-rich suboxic-diagenetic layer growth structures of a deeply buried nodule (SO240-22KL-801cm).

Figure 11 a: Comparison between Ni and Cu Fourier transformed (FT) EXAFS measurements of a nodule from the sediment surface (21KG). The amplitude of the second peak (Ni-Mn) of Ni FT is more intense than that of Cu FT (Cu-Mn), which results from the difference of the number of neighbor atoms around the metal (Ni or Cu). Higher amplitude is characteristic for more neighbors (b). b: Model of incorporation of Ni and Cu in the [MnO_6]-octahedral sheets of phyllomanganates of surface nodules. Only the incorporation of Ni and Cu is shown in the model because the proportion of Cu and Ni sorbed as triple-corner sharing complexes versus vacancies in phyllomanganates is very small.

Figure 12 a: Comparison between Ni and Cu Fourier transformed (FT) EXAFS measurements of a deeply buried nodule (65SL-985cm). The amplitude of the second peak of Ni FT (Ni-Mn) is more intense than that of Cu FT (Cu-Mn) due to the higher number of neighboring atoms. **b:** Model of the incorporation of Ni, Cu and Co into the todorokite structure of deeply buried nodules. Ni and Co can be incorporated in the middle of the three octahedra chains of the todorokite tunnel, minor amounts of Ni can be also incorporated on the edges of the octahedra chains. Cu and Ni can also be located as outer-sphere complex within the todorokite tunnel structure.

Figure 13: Cu *K*-edge EXAFS spectra of surface, subsurface and deeply buried nodules compared with different Cu *K*-edge EXAFS measurements of Manceau et al. (2014). The arrow at 5.5 k $Å^{-1}$ mark the differences between the individual samples. **b:** Cu FT EXAFS measurements of surface, subsurface, and deeply buried nodules compared with data of Manceau et al. (2014).

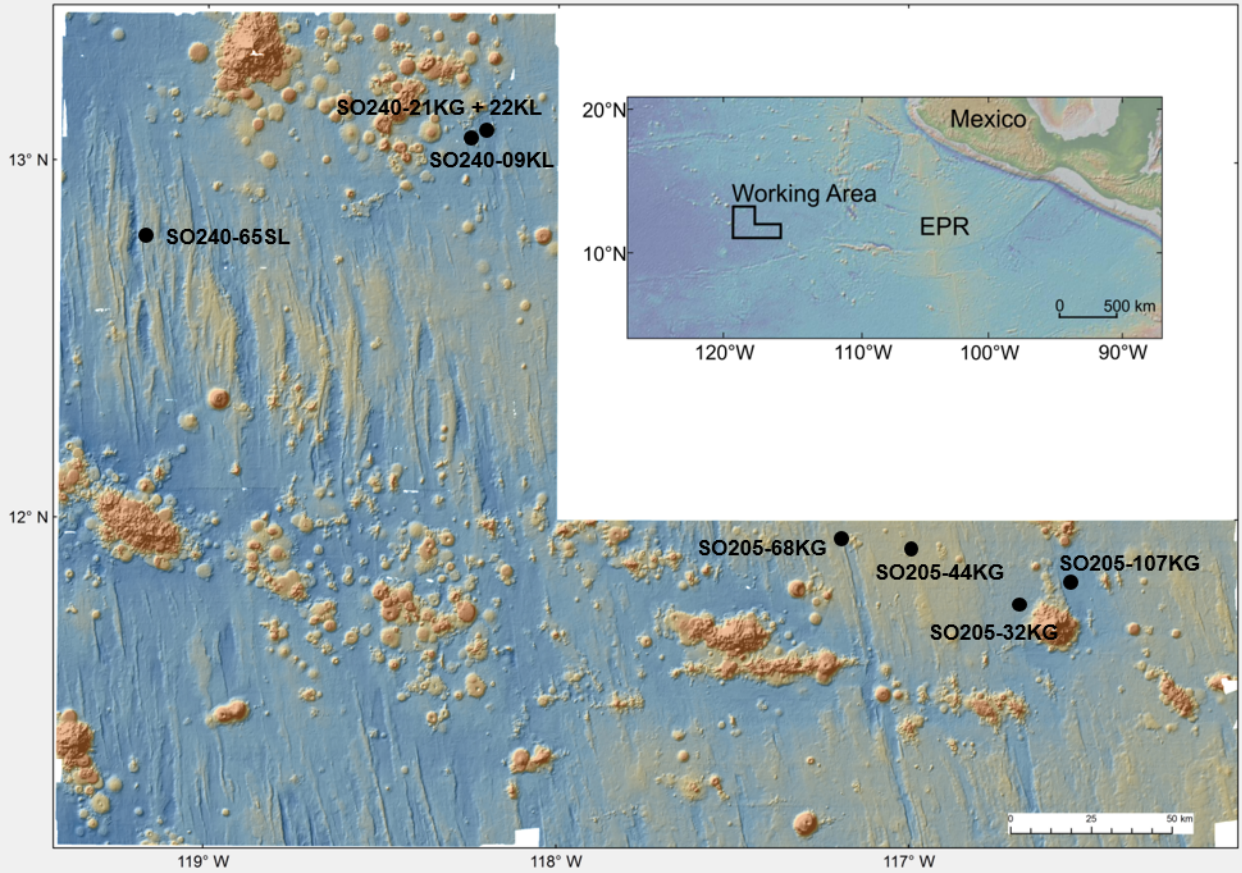
SO240-21KG + 22KL
SO240-09KL
SO240-65SL
SO205-68KG
SO205-44KG
SO205-107KG
SO205-32KG
13° N
12° N
119° W
118° W
117° W
0 25 50 km
20°N
10°N
120°W
110°W
100°W
90°W
Mexico
Working Area
EPR
0 500 km

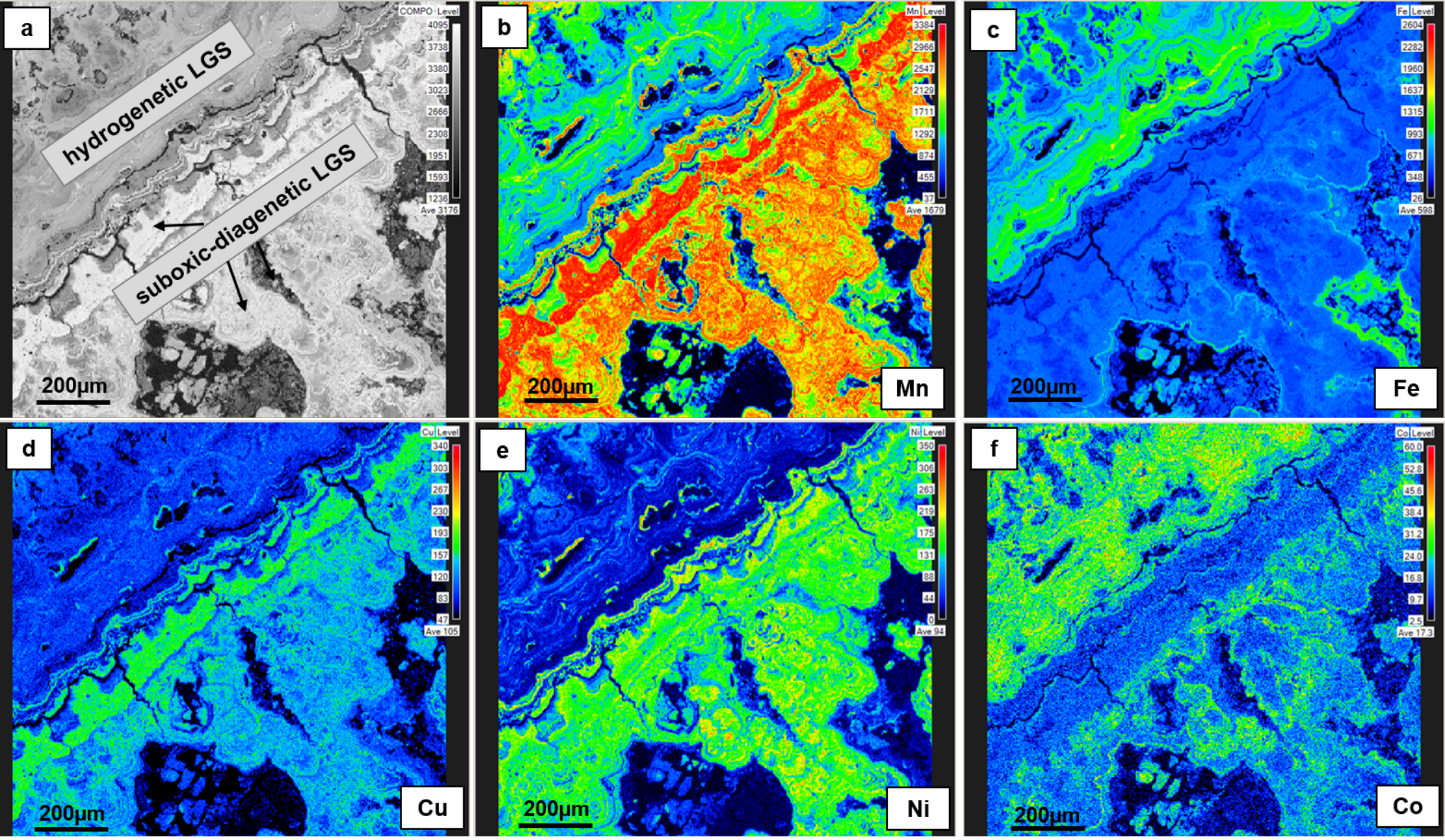
a
hydrogenetic LGS
suboxic-diagenetic LGS
200μm
b
Mn
200μm
c
Fe
200μm
d
Cu
200μm
e
Ni
200μm
f
Co
200μm

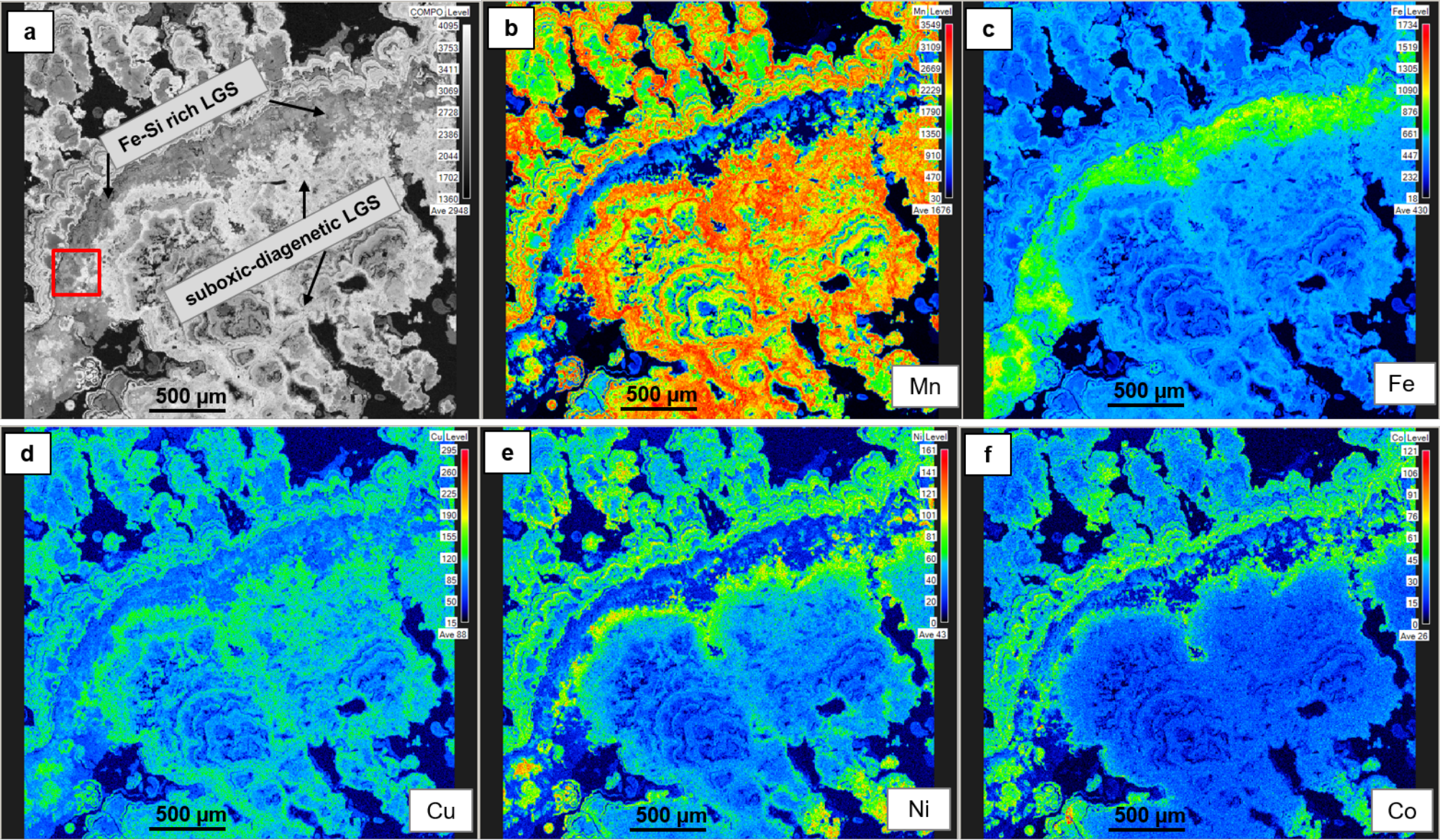
a
COMPO Level
4095
3753
3411
3069
2728
2386
2044
1702
1360
Ave 2948
Fe-Si rich LGS
suboxic-diagenetic LGS
500 µm
b
Mn Level
3549
3109
2669
2229
1790
1350
910
470
30
Ave 1676
500 µm
Mn
c
Fe Level
1734
1519
1305
1090
876
661
447
232
18
Ave 430
500 µm
Fe
d
Cu Level
295
260
225
190
155
120
85
50
15
Ave 88
500 µm
Cu
e
Ni Level
161
141
121
101
81
60
40
20
0
Ave 43
500 µm
Ni
f
Co Level
121
106
91
76
61
45
30
15
0
Ave 26
500 µm
Co

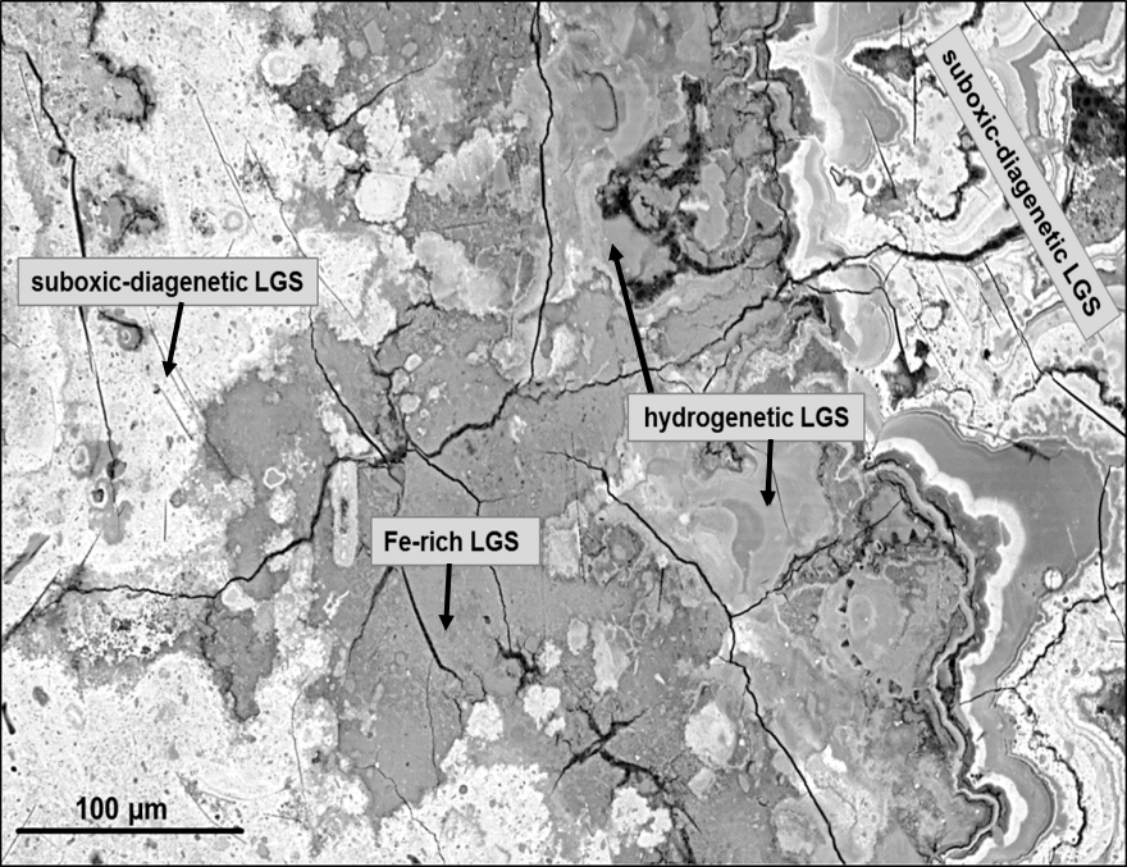
suboxic-diagenetic LGS
suboxic-diagenetic LGS
hydrogenetic LGS
Fe-rich LGS
100 µm

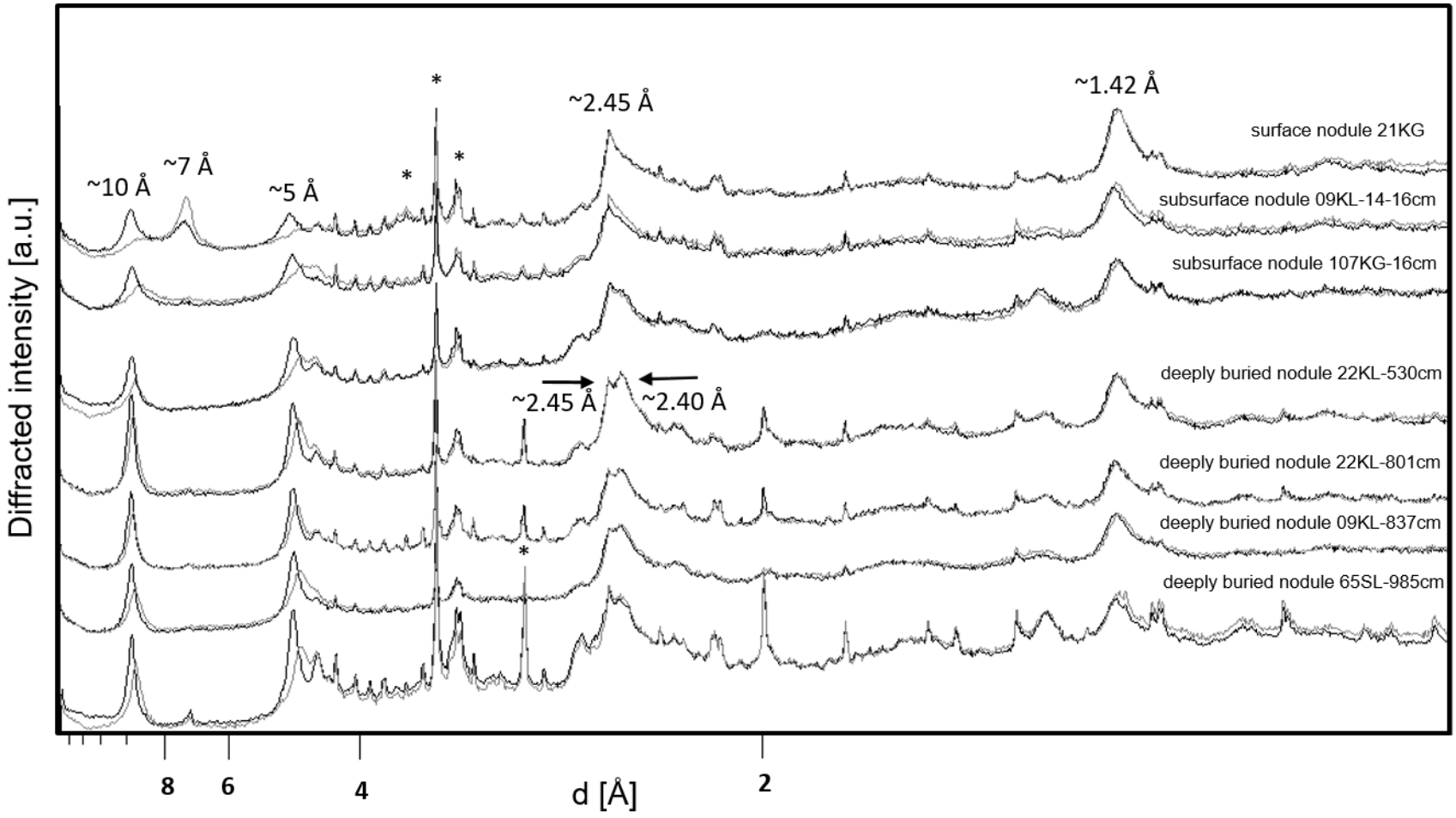
Diffracted intensity [a.u.]
~10 Å
~7 Å
~5 Å
*
*
*
~2.45 Å
~1.42 Å
surface nodule 21KG
subsurface nodule 09KL-14-16cm
subsurface nodule 107KG-16cm
deeply buried nodule 22KL-530cm
~2.45 Å
~2.40 Å
deeply buried nodule 22KL-801cm
deeply buried nodule 09KL-837cm
*
deeply buried nodule 65SL-985cm
8
6
4
d [Å]
2

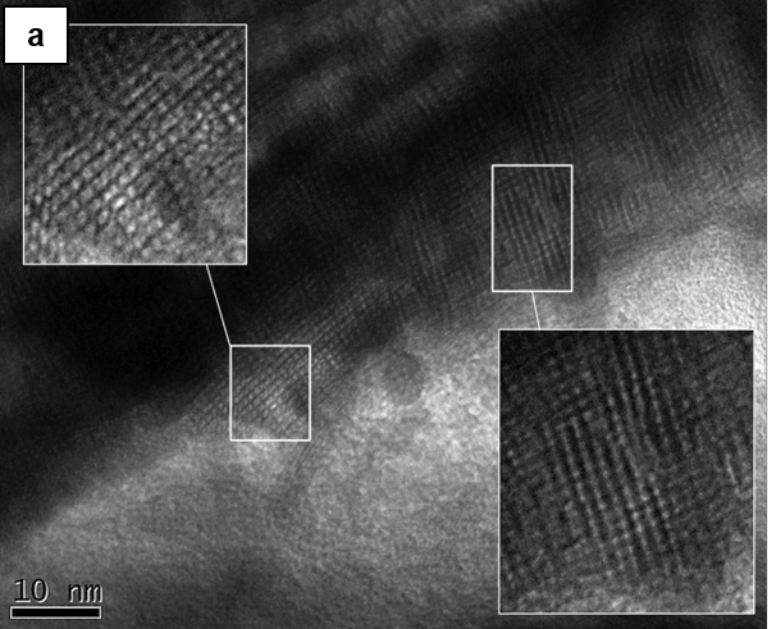
a
10 nm

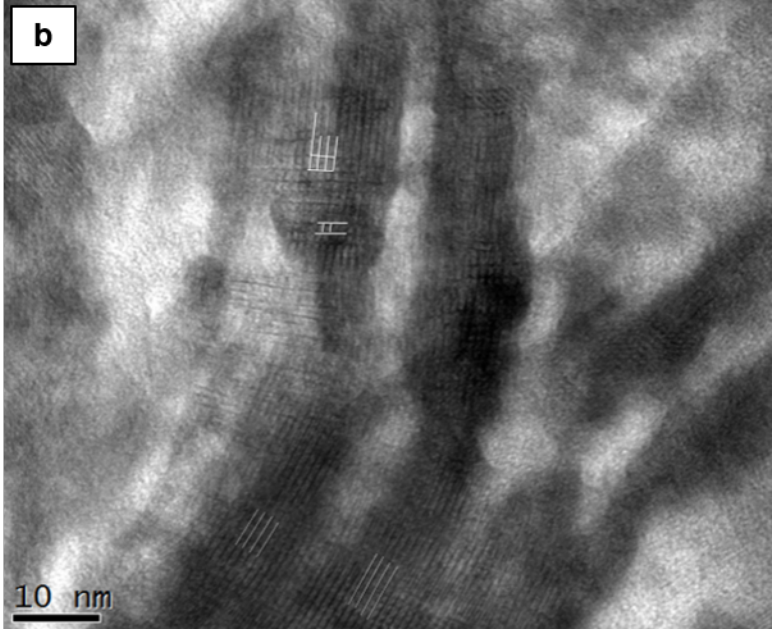
b
10 nm

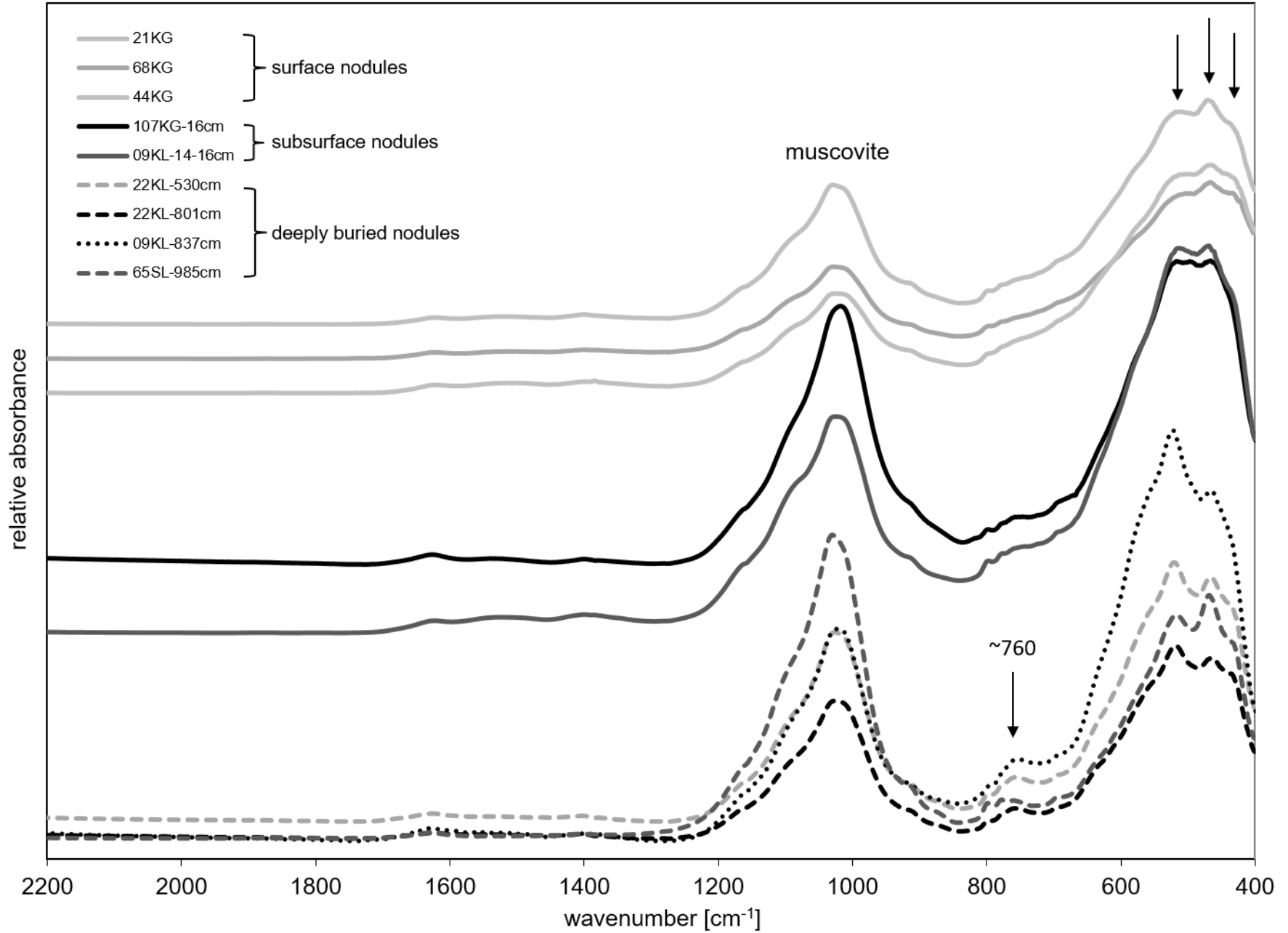
21KG
68KG
44KG
surface nodules
107KG-16cm
09KL-14-16cm
subsurface nodules
22KL-530cm
22KL-801cm
09KL-837cm
65SL-985cm
deeply buried nodules
muscovite
~760
relative absorbance
2200
2000
1800
1600
1400
1200
1000
800
600
400
wavenumber [cm-1]

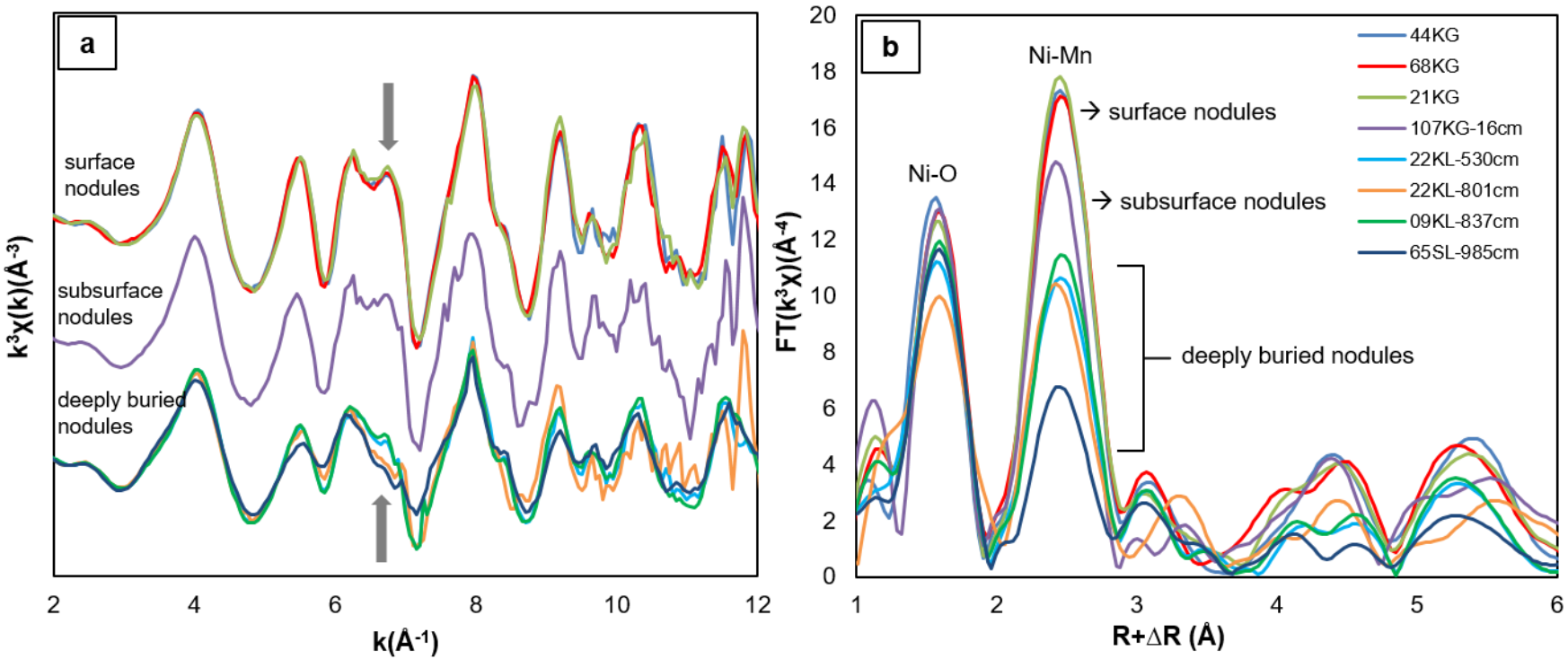
a
surface nodules
subsurface nodules
deeply buried nodules
k³χ(k)(Å⁻³)
k(Å⁻¹)
2
4
6
8
10
12
b
Ni-Mn
Ni-O
→ surface nodules
→ subsurface nodules
deeply buried nodules
FT(k³χ)(Å⁻⁴)
R+ΔR (Å)
0
2
4
6
8
10
12
14
16
18
20
1
2
3
4
5
6
44KG
68KG
21KG
107KG-16cm
22KL-530cm
22KL-801cm
09KL-837cm
65SL-985cm

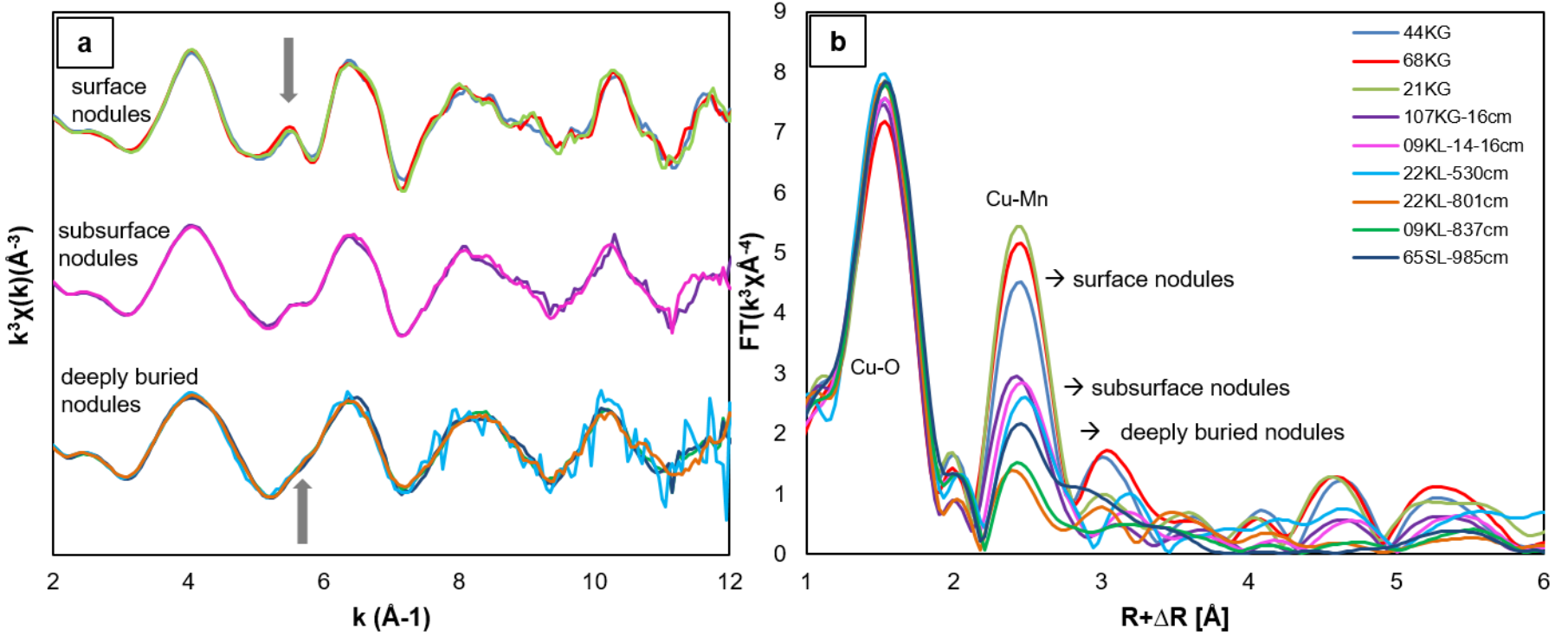
a
surface nodules
subsurface nodules
deeply buried nodules
k³χ(k)(Å⁻³)
2
4
6
8
10
12
k (Å-1)
b
44KG
68KG
21KG
107KG-16cm
09KL-14-16cm
22KL-530cm
22KL-801cm
09KL-837cm
65SL-985cm
Cu-Mn
Cu-O
→ surface nodules
→ subsurface nodules
→ deeply buried nodules
FT(k³χÅ⁻⁴)
0
1
2
3
4
5
6
7
8
9
1
2
3
4
5
6
R+ΔR [Å]

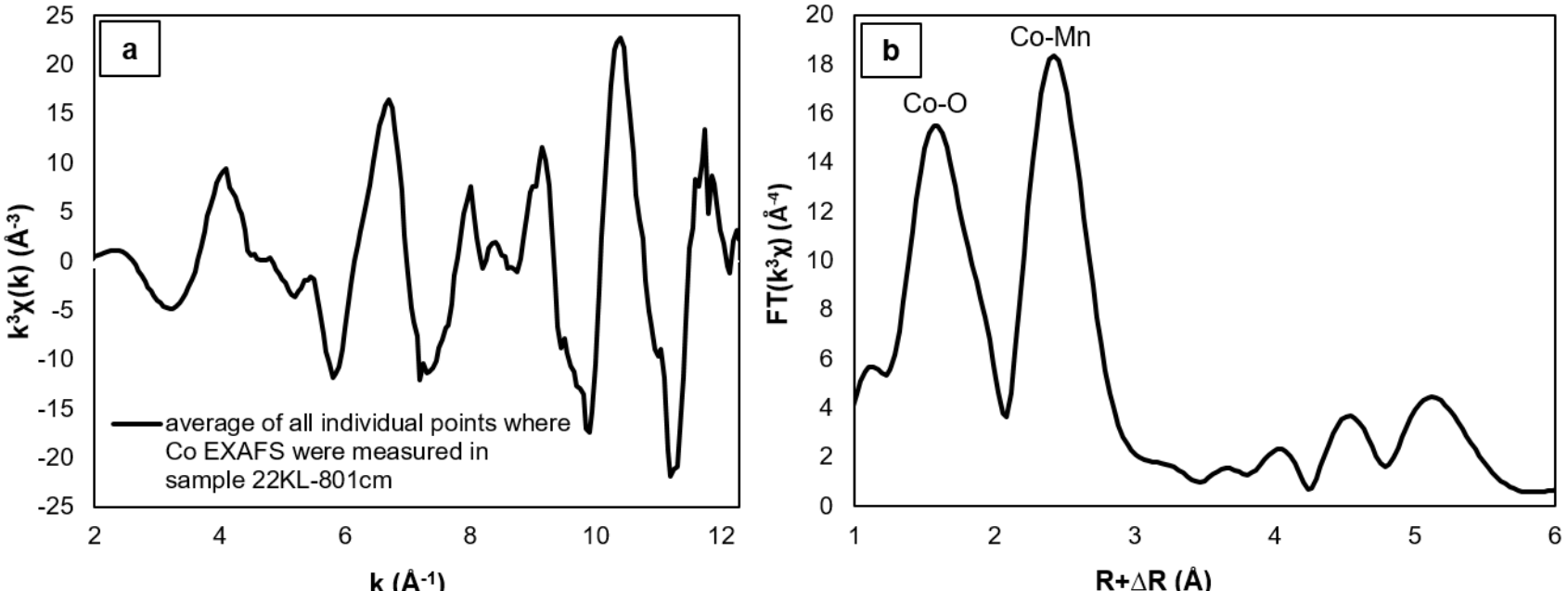
a
b
Co-O
Co-Mn
average of all individual points where Co EXAFS were measured in sample 22KL-801cm
k³χ(k) (Å⁻³)
k (Å⁻¹)
FT(k³χ) (Å⁻⁴)
R+ΔR (Å)

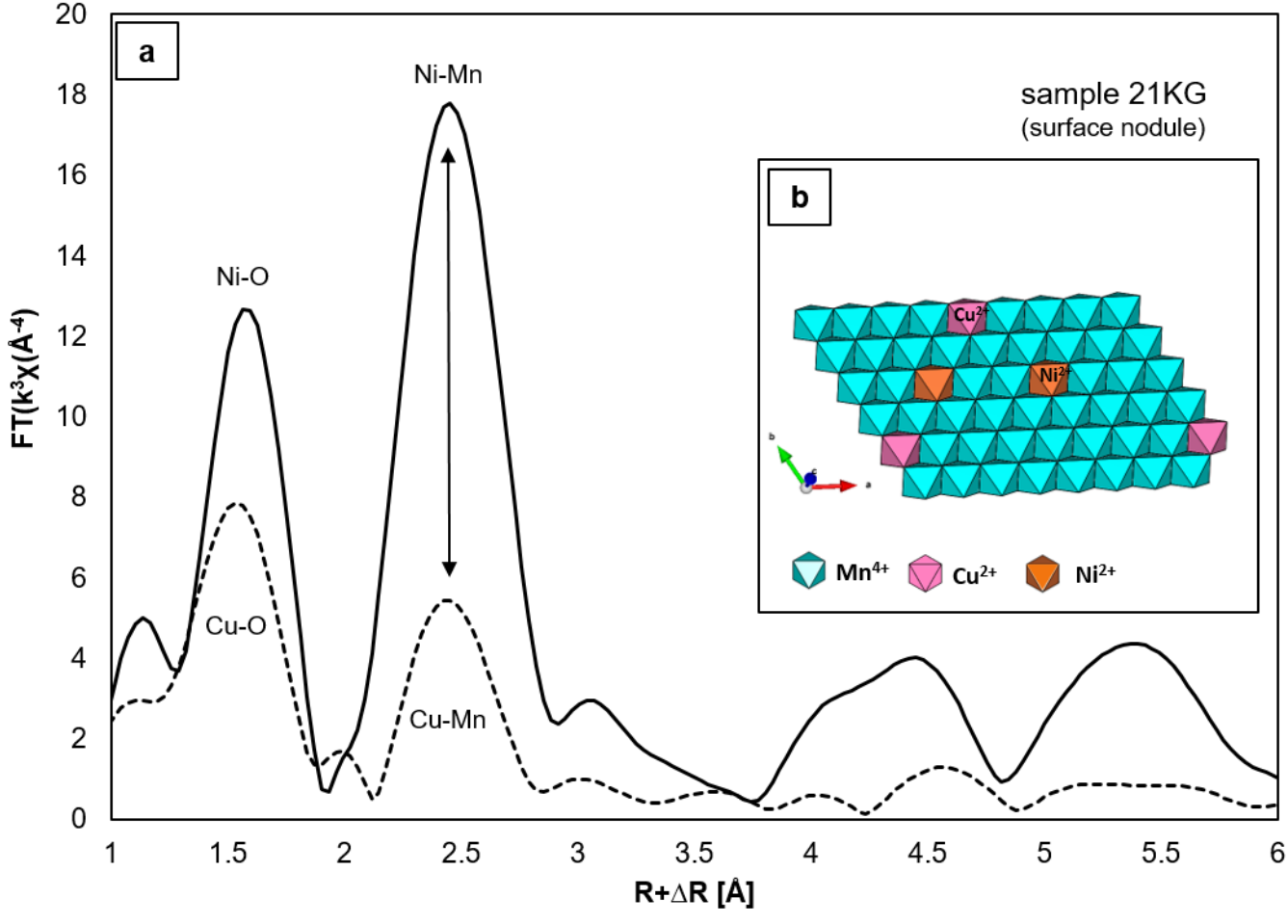
a
Ni-Mn
Ni-O
Cu-O
Cu-Mn
sample 21KG
(surface nodule)
b
Cu2+
Ni2+
Mn4+
Cu2+
Ni2+
FT(k3χ(Å-4)
R+ΔR [Å]
0
2
4
6
8
10
12
14
16
18
20
1
1.5
2
2.5
3
3.5
4
4.5
5
5.5
6

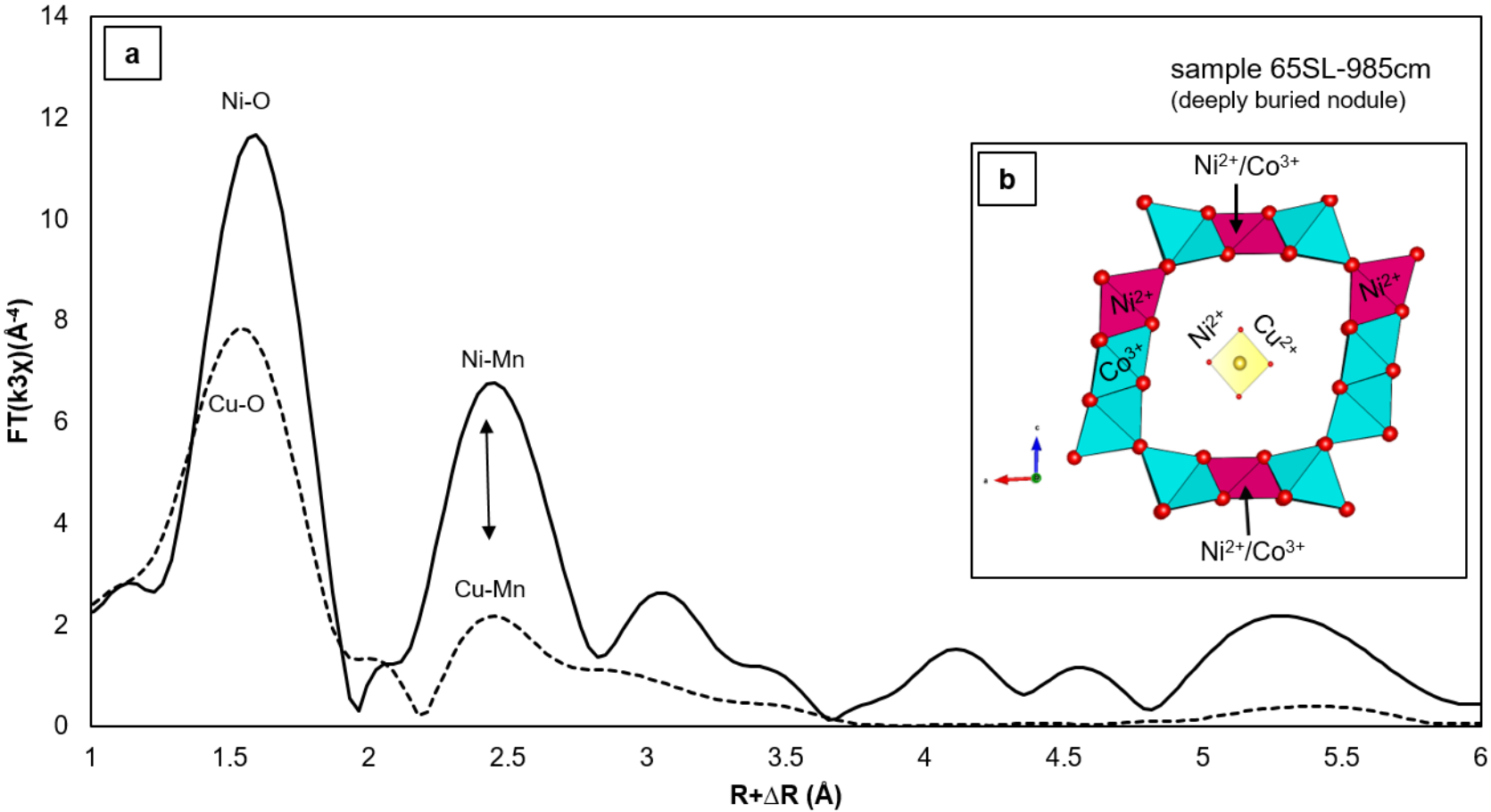
a
sample 65SL-985cm
(deeply buried nodule)
Ni-O
Cu-O
Ni-Mn
Cu-Mn
FT(k3χ)(Å⁻⁴)
R+ΔR (Å)
b
Ni2+/Co3+
Ni2+
Ni2+
Ni2+
Co3+
Cu2+
Ni2+/Co3+

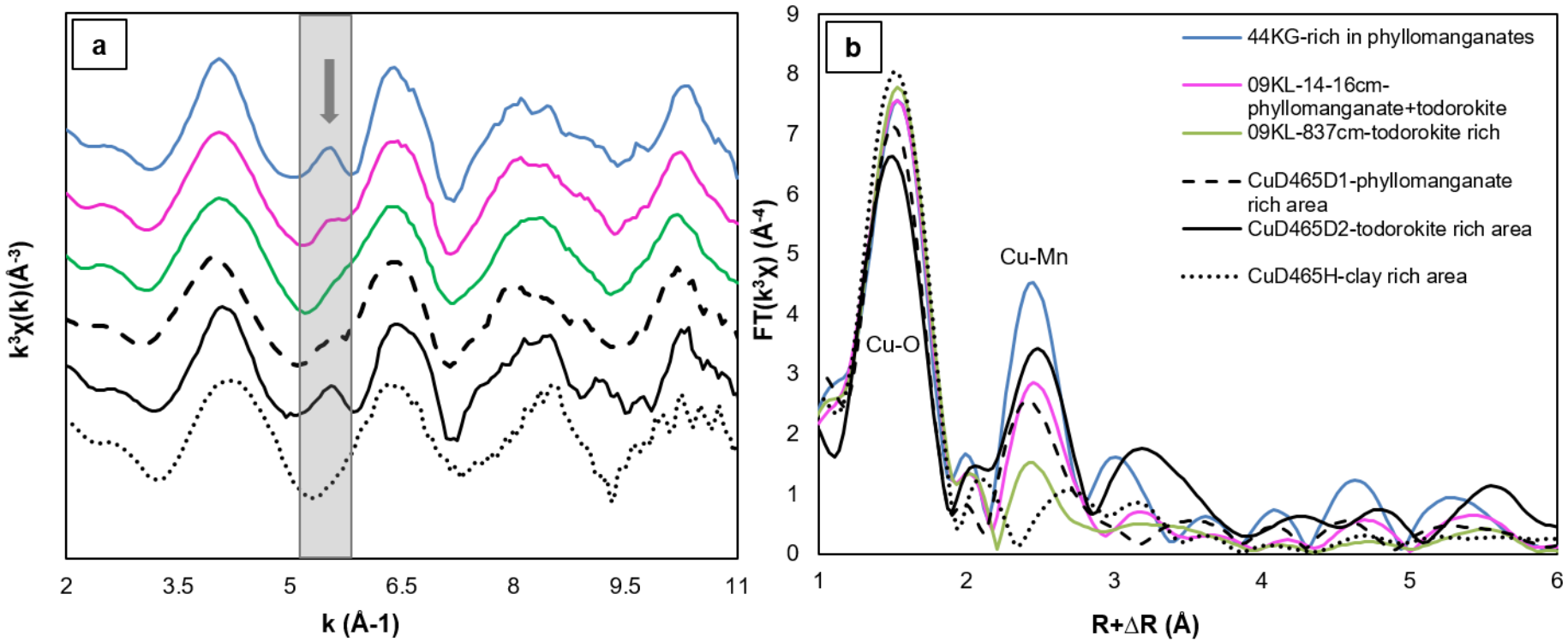
a
b
k³χ(k)(Å⁻³)
k (Å-1)
2
3.5
5
6.5
8
9.5
11
FT(k³χ) (Å⁻⁴)
R+ΔR (Å)
1
2
3
4
5
6
0
1
2
3
4
5
6
7
8
9
Cu-O
Cu-Mn
44KG-rich in phyllomanganates
09KL-14-16cm-phyllomanganate+todorokite
09KL-837cm-todorokite rich
CuD465D1-phyllomanganate rich area
CuD465D2-todorokite rich area
CuD465H-clay rich area

Table 1: EXAFS fits for Ni in surface, subsurface and deeply buried bulk nodules from the CCZ.

sample	nodule location	shell	R (Å)	δ^2(Å^2)	CN	E (%)	TC(%)	E_0 (eV)	R-factor
44KG	sediment surface	Ni-O	2.01	0.003	6.0	85	15	-4.55	0.02
		Ni-Mn (E)	2.84	0.004	5.1				
		Ni-Mn (TC)	3.49	-0.001	0.9				
68KG	sediment surface	Ni-O	2.03	0.004	6.0	100		-0.31	0.02
		Ni-Mn (E)	2.87	0.004	6.0				
21KG	sediment surface	Ni-O	2.03	0.004	6.0	100		-0.47	0.02
		Ni-Mn (E)	2.86	0.004	6.0				
107KG-16cm	buried, 16 cmbsf	Ni-O	2.03	0.004	6.0	100		-3.24	0.03
		Ni-Mn (E)	2.86	0.005	5.7				
22KL-530cm	buried, 530 cmbsf	Ni-O	2.04	0.005	6.0	76	24	-0.24	0.01
		Ni-Mn (E)	2.87	0.005	4.6				
		Ni-Mn (TC)	3.57	0.009	1.4				
22KL-801cm	buried, 801 cmbsf	Ni-O	2.05	0.006	6.0	68	32	-0.81	0.06
		Ni-Mn (E)	2.88	0.005	4.1				
		Ni-Mn (TC)	4.00	0.005	1.9				
09KL-837cm	buried, 837 cmbsf	Ni-O	2.04	0.004	6.0	75	25	0.01	0.01
		Ni-Mn (E)	2.88	0.005	4.5				
		Ni-Mn (TC)	3.58	0.010	1.5				
65SL-985cm	buried, 985 cmbsf	Ni-O	2.04	0.005	6.0	35	65	-1.17	0.02
		Ni-Mn (E)	2.87	0.003	2.1				
		Ni-Mn (TC)	3.55	0.016	3.9				

E = edge-sharing complex = metals incorporation into the manganese layer sheets;
TC = triple corner sharing complex = metals adsorption above/below vacancy sites of phyllomanganate sheets;
CN=coordination number; R=binding distance; δ=Debye Weller factor (The Debye-Waller factor describes the attenuation of x-ray scattering or coherent neutron scattering caused by thermal motion. It is temperature dependent and characteristic for individual elements); E0=energy shift; R-factor = goodness of fit parameter; cmbsf = centimeters below seafloor

Table 2: EXAFS fits for Cu in surface bulk nodules from the CCZ.

sample	nodule location	shell	R (Å)	δ^2(Å^2)	CN	E_0 (eV)	R-factor
44KG	sediment surface	Cu-O	1.96	0.004	3.6	-0.80	0.01
		Cu-Mn (E)	2.87	0.007	1.9		
		Cu-Mn (TC)	3.42	0.007	1.3		
68KG	sediment surface	Cu-O	1.96	0.005	3.7	-1.00	0.01
		Cu-Mn (E)	2.87	0.008	2.5		
		Cu-Mn (TC)	3.45	0.008	1.6		
21KG	sediment surface	Cu-O	1.96	0.003	3.3	-0.38	0.01
		Cu-Mn (E)	2.88	0.007	2.6		
		Cu-Mn (TC)	3.45	0.007	0.9		

Table 3: EXAFS fit for Co in individual Co-rich suboxic-diagenetic growth structures of a buried nodule (22KL-801cm) from the CCZ.

sample	nodule location	shell	R (Å)	δ^2 (Å^2)	CN	E0 (eV)	R-factor
22KL-801cm	buried, 801 cmbsf	Co-O1	1.94	0.001	6.0	1.17	0.02
		Co-O2	2.25	0.001	2.6		
		Co-Mn1 (E)	2.88	0.002	6.0		
		Co-Mn2	3.08	0.002	2.2		